

MAGS-SLAM: Monocular Multi-Agent Gaussian Splatting SLAM for Geometrically and Photometrically Consistent Reconstruction

Zhihao Cao*
ETH Zurich
Zurich, Switzerland
zhicao@ethz.ch

Qi Shao*
Harbin Engineering University
Harbin, China
University of Liverpool
Liverpool, United Kingdom
shaoqi9@hrbeu.edu.cn

Shuhao Zhai*
University of Macau
Macao(SAR), China
University of Ottawa
Ottawa, Canada
mc35379@um.edu.mo

Jing Zhang
Wuhan University
Wuhan, China
jingzhang.cv@gmail.com

Anh Nguyen
University of Liverpool
Liverpool, United Kingdom
anh.nguyen@liverpool.ac.uk

Baoru Huang[†]
University of Liverpool
Liverpool, United Kingdom
Imperial College London
London, United Kingdom
baoru.huang@liverpool.ac.uk

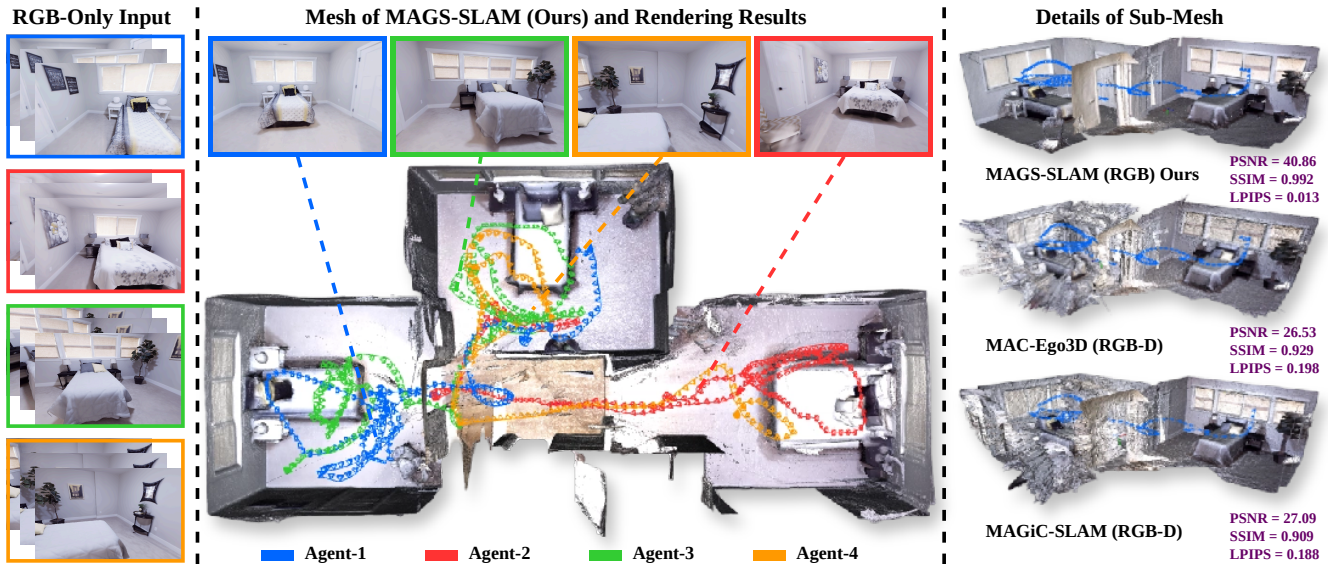


Figure 1: Overview of MAGS-SLAM. MAGS-SLAM reconstructs a globally consistent photorealistic 3D Gaussian map from multiple agents using only RGB video, without depth sensors or post-processing. Compared with state-of-the-art RGB-D multi-agent Gaussian SLAM systems, our method achieves competitive or superior novel-view synthesis quality while avoiding active depth sensing, and yields cleaner multi-agent fusion with reduced misalignment, duplicated Gaussians, and photometric seams.

<https://mags-slam.github.io>

Abstract

Collaborative photorealistic 3D reconstruction from multiple agents enables rapid large-scale scene capture for virtual production and cooperative multi-robot exploration. While recent 3D Gaussian Splatting (3DGS) SLAM algorithms can generate high-fidelity real-time mapping, most of the existing multi-agent Gaussian SLAM

methods still rely on RGB-D sensors to obtain metric depth and simplify cross-agent alignment, which limits the deployment on lightweight, low-cost, or power-constrained robotic platforms. To address this challenge, we propose MAGS-SLAM, the first RGB-only multi-agent 3DGS SLAM framework for collaborative scene reconstruction. Each agent independently builds local monocular Gaussian submaps and transmits compact submap summaries

*These authors contributed equally to this research.

[†] Corresponding author.

rather than raw observations or dense maps. To facilitate robust collaboration in the presence of monocular scale ambiguity, our framework integrates compact submap communication, geometry- and appearance-aware loop verification, and occupancy-aware Gaussian fusion, enabling coherent global reconstruction without active depth sensors. We further introduce ReplicaMultiagent Plus benchmark for evaluating collaborative Gaussian SLAM. Intensive experiments on synthetic and real-world datasets show that MAGS-SLAM achieves competitive tracking accuracy and comparable or superior rendering quality to state-of-the-art RGB-D collaborative Gaussian SLAM methods while relying only RGB images.

1 Introduction

Collaborative photorealistic 3D reconstruction from multiple agents enables rapid large-scale scene capture, critical for virtual production, immersive telepresence, multi-user augmented reality, and cooperative multi-robot exploration. Recently, 3D Gaussian Splatting (3DGS) [18] has emerged as a powerful representation for real-time photorealistic scene reconstruction and dense visual SLAM. As an explicit, differentiable, and real-time renderable scene representation, 3DGS supports efficient map optimization and high-fidelity novel-view synthesis, motivating a rapidly growing family of single-agent Gaussian SLAM systems [10, 11, 15, 17, 23, 27, 32, 36, 50, 54, 59]. However, a single camera observes only a limited portion of an environment at any time, rendering sequential capture inefficient for large-scale or multi-room scenes. Multi-agent collaborative SLAM addresses this bottleneck by enabling parallel exploration, complementary viewpoints, and redundant observations. Early collaborative SLAM systems mainly focused on sparse geometric maps [20, 21, 37, 46], while recent methods have extended collaboration to renderable neural implicit and Gaussian representations [4–6, 12, 45, 49, 53]. Nevertheless, existing multi-agent 3DGS systems still require RGB-D sensors to obtain metric depth and simplify inter-agent alignment to rigid SE(3) registration. This dependence on active depth sensing increases hardware cost, power consumption, calibration complexity, and synchronization overhead, limiting deployment on lightweight or heterogeneous robotic platforms. Consequently, monocular RGB-only multi-agent Gaussian SLAM remains a critical open challenge, as monocular agents reconstruct local Gaussian maps with inherent scale ambiguity and uncertain cross-agent overlaps.

To address this gap, we propose **MAGS-SLAM**, the first monocular RGB-only multi-agent 3DGS SLAM framework for collaborative photorealistic reconstruction. Each agent independently estimates monocular poses and depths, incrementally constructs local Gaussian submaps, and communicates compact submap summaries instead of raw observations or dense maps. To bridge independently scaled monocular maps, a communication-efficient coordinator establishes reliable cross-agent Sim(3) constraints from compact submap summaries through descriptor retrieval, spatially well-conditioned geometric verification, and sparse-cloud refinement. These constraints define a global Sim(3) submap graph that aligns monocular reconstructions with both geometric and photometric consistency. An asynchronous occupancy-aware fusion stage then fuses the aligned Gaussian submaps, filtering redundant Gaussians while preserving observed free space, followed by

joint pose-Gaussian photometric refinement. The resulting system achieves competitive tracking accuracy and collaborative photorealistic reconstruction without any depth sensors.

Our main contributions are:

- (1) We propose the first monocular RGB-only multi-agent 3D Gaussian Splatting SLAM system. It integrates Gaussian front-ends, compact submap summaries, inter-agent verification, Sim(3) submap pose graph, and occupancy-aware fusion into a unified framework, achieving accurate tracking and photorealistic reconstruction without depth sensors.
- (2) We propose a Pose-Graph Bundle Adjustment (PGBA)-consistent Sim(3) loop closure mechanism for multi-agent systems, which jointly resolves intra- and inter-agent scale drift through a submap-level Sim(3) pose graph coupling geometric and photometric residuals. Robustness is ensured by a spatial-extent gate that rejects degenerate loops and an adaptive edge invalidation scheme consistent with evolving PGBA corrections.
- (3) We propose an occupancy-aware fusion framework for coherent multi-agent Gaussian maps. It combines occupancy-grid deduplication, decoupled coordinator, and joint pose-Gaussian photometric refinement to eliminate duplicated Gaussians, residual misalignment, and photometric seams across agents.
- (4) We introduce **ReplicaMultiagent Plus** dataset. While existing multi-agent datasets are typically limited to 2-3 agents with short trajectories, our dataset scales to 4 agents with long-horizon trajectories. In addition, we provide ground-truth geometry and semantic annotations, supporting the evaluation of monocular, RGB-D, and semantic multi-agent SLAM for collaborative dense reconstruction.

2 Related Work

2.1 Dense and Photorealistic Visual SLAM

Visual SLAM systems have progressively expanded from accurate camera tracking toward dense, photorealistic scene reconstruction. Sparse tracking systems such as ORB-SLAM3 [2] and DSO [7] provide accurate camera poses but limited scene geometry, while dense or semi-dense direct methods such as DTAM [29] and LSD-SLAM [8] improve reconstruction density. Recent learning-based systems, including DROID-SLAM [43], DPVO [44], and MAST3R-SLAM [28], further improve correspondence estimation, bundle adjustment, and monocular reconstruction with learned priors.

Neural implicit SLAM methods [16, 26, 34, 35, 41, 48, 51, 56, 57, 60, 61] enable high-fidelity geometry and appearance reconstruction, but volume rendering and neural optimization limit real-time scalability. 3D Gaussian Splatting (3DGS) [18] and surface-oriented variants such as 2DGS [14] provide explicit differentiable primitives with efficient rasterization and have been adopted in single-agent Gaussian SLAM [10, 11, 17, 23, 27, 32, 36, 50, 54, 55, 59]. These methods achieve photorealistic reconstruction from monocular or RGB-D input, but do not address inter-agent coordination, cross-agent scale alignment, or duplicate-aware Gaussian fusion.

2.2 Multi-Agent Collaborative SLAM

Multi-agent collaborative SLAM addresses single-agent coverage limitations through parallel exploration, inter-agent loop closure,

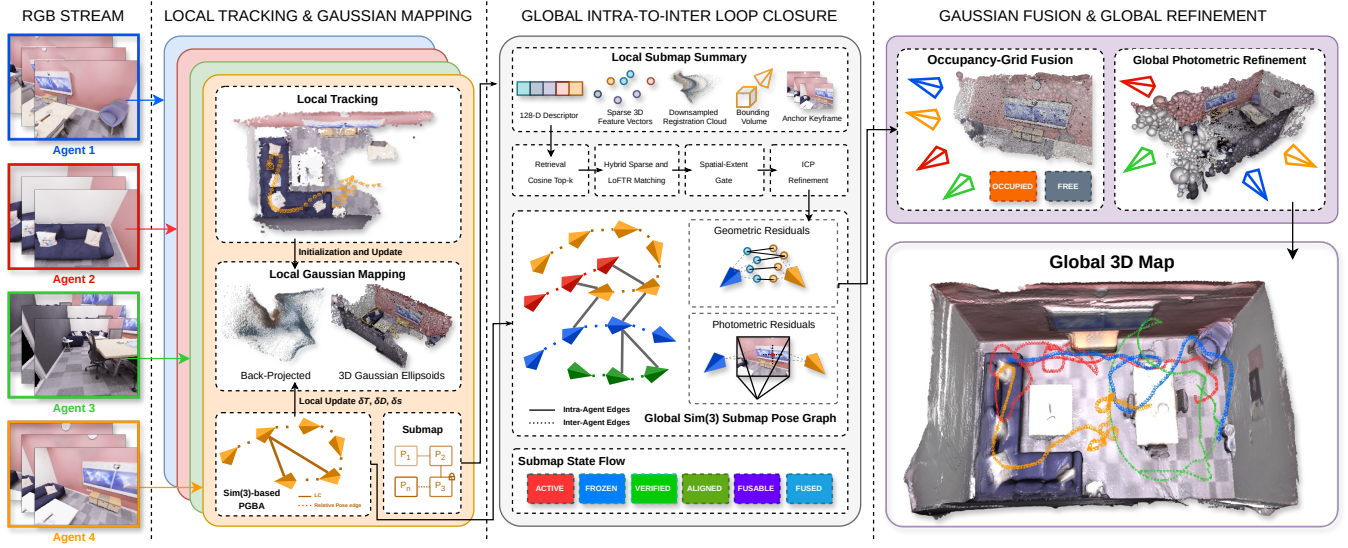


Figure 2: MAGS-SLAM Pipeline. Each agent runs JDSA-coupled dense BA on its RGB stream, back-projects inverse depth into 3D Gaussian ellipsoids, and groups keyframes into bounded submaps frozen; intra-agent loops trigger Sim(3) PGBA with relative-pose edges. Then, each frozen submap is encoded as a 128-D descriptor, sparse 3D feature points, a registration cloud, and a downsampled anchor keyframe; cosine top- k retrieval, hybrid sparse and LoFTR matching with RANSAC and Umeyama Sim(3) quite several technical terms are not defined or cited clearly/correctly in the first time it is shown, a spatial-extent gate, and ICP refinement produce verified inter-agent constraints, which are jointly optimized with intra-agent temporal edges in a global Sim(3) submap pose graph under geometric r^{geo} and anchor-image photometric r^{pho} residuals. Finally, an occupancy-grid fusion deduplicates borrowed Gaussians against each target agent’s occupied and free-space voxels, after which a joint photometric refinement of fused Gaussians, keyframe poses, and exposures produces the final globally consistent photorealistic map.

and submap sharing. Sparse collaborative frameworks [20, 21, 37, 38, 46] support trajectory alignment and distributed optimization, but are not designed for photorealistic rendering. Neural-field extensions [5, 6, 12] reduce communication overhead, yet inherit the rendering and scalability limits of implicit representations.

Recent 3DGS-based collaborative systems [4, 45, 49, 52, 53] enable renderable maps, but typically rely on RGB-D input, where metric depth simplifies inter-agent alignment to rigid SE(3). In monocular settings, independently optimized agents can produce inconsistent scales, requiring Sim(3) alignment and duplicate-aware fusion to avoid redundant Gaussians and density inconsistencies.

Among RGB-only baselines, the MultiSLAM-DiffPose [25] yields only sparse geometry, the MANG-SLAM [24] treats 3DGS as a downstream renderer guided by NeRF submap priors rather than a native representation, and the MA-MASt3R-SLAM [58] performs dense monocular map fusion with 3D reconstruction priors but does not exploit the explicit and differentiable renderable representation of 3DGS. Monocular RGB-only collaborative 3DGS SLAM with scale-consistent Sim(3) alignment and Gaussian fusion therefore remains underexplored.

3 MAGS-SLAM

Our MAGS-SLAM framework provides a monocular RGB-only multi-agent 3D Gaussian Splatting SLAM system (Fig. 2). Each agent runs an independent monocular RGB-only front-end that builds local Gaussian submaps, while a lightweight coordinator

discovers overlaps from compact submap summaries, maintains a global Sim(3) pose graph, and performs occupancy-aware fusion.

3.1 Local Per-Agent Monocular Gaussian SLAM

Each agent runs an independent monocular DROID-based [43] front-end that couples recurrent dense bundle adjustment with a learned monocular depth prior [13]. Over a sliding co-visibility window, poses $\{T\}$ and depth maps $\{d\}$ are refined by minimizing among keyframe graph $\mathcal{G} = (\mathcal{V}, \mathcal{E})$

$$\mathcal{L}^{\text{BA}} = \sum_{(i,j) \in \mathcal{E}} \left\| \mathbf{u}_{ij}^* - \pi(T_{ij} \pi^{-1}(\mathbf{u}_i, \mathbf{d}_i)) \right\|_{\Sigma_{ij}}^2, \quad (1)$$

where \mathbf{u}^* is the refined correspondence [43], and π and π^{-1} are the camera projection operators. To improve monocular scale consistency from monocular input, scale coefficients $\{s\}$ and depth maps $\{d\}$ are jointly minimizing via Joint Depth-Scale Adjustment (JDSA) [3, 55, 56]

$$\mathcal{L}^{\text{JDSA}} = \mathcal{L}^{\text{BA}} + \sum_{k \in \mathcal{V}} \left\| \mathcal{B}_k \mathbf{d}_k - \mathbf{d}_k^{\text{prior}} \right\|^2, \quad (2)$$

where $\mathbf{d}_k^{\text{prior}}$ is a learned depth prior from Metric3D [13], and $\mathcal{B}_k(\mathbf{u}_k, \mathbf{s}_k)$ is a bilinear interpolation on the grid based on its four surrounding grid coefficients to adjust the depth. Intra-agent loop closure (LC) candidates trigger online Sim(3) pose-graph bundle adjustment (PGBA) [55, 62] over the full keyframe history to maintain short-

and long-consistency via

$$\mathcal{L}^{\text{PGBA}} = \mathcal{L}^{\text{BA}^*} + \sum_{(i,j) \in \mathcal{E}^+} \|\log(\hat{\mathbf{T}}_{ij} \mathbf{T}_i \mathbf{T}_j^{-1})\|_{\Sigma_{ij}^+}^2. \quad (3)$$

Here, $\mathcal{L}^{\text{BA}^*}$ is with \mathcal{G}^* , where \mathcal{E}^* in \mathcal{G}^* is the loop edges based on optical flow differences. \mathcal{E}^+ is the relative pose graph by adding the relative pose from graph \mathcal{G} . $\hat{\mathbf{T}}_{ij}$ is the relative pose in the pose graph. When a new keyframe is registered, its inverse-depth map is back-projected to seed new Gaussians. Each Gaussian is initialized with center $\boldsymbol{\mu} = \mathbf{T}_k^{-1} \pi^{-1}(\mathbf{u}, \mathbf{d}_k)$, color from the pixel, and scale from the local neighborhood. The local Gaussian map is then optimized against a sliding window of keyframes by gradient descent on

$$\mathcal{L}^{\text{map}} = \alpha \mathcal{L}_1(\hat{I}, I) + \beta \mathcal{L}_1(\hat{D}, D) + \lambda_n \mathcal{L}_{\text{normal}} + \lambda_s \mathcal{L}_{\text{iso}}, \quad (4)$$

with weights $\alpha = 0.95$, $\beta = 0.25$, $\lambda_n = 10^{-2}$, $\lambda_s = 10$. The photometric and depth terms reduce to per-keyframe L1 errors over the sliding window \mathcal{K} , where D denotes the BA-estimated depth used as self-supervision. The normal term $\mathcal{L}_{\text{normal}} = \sum_{k \in \mathcal{K}} |1 - \hat{N}_k^\top \bar{N}_k|$ is a cosine embedding loss between the depth-induced normal \hat{N}_k and the monocular normal prior \bar{N}_k , and the regularizer $\mathcal{L}_{\text{iso}} = \sum_{i \in \mathcal{G}} |\mathbf{s}_i - \bar{\mathbf{s}}_i|$ pulls each Gaussian’s scale components toward their mean $\bar{\mathbf{s}}_i$ to penalize ellipsoid stretching. The optimization above runs continuously over a sliding keyframe window. To interface with the inter-agent coordinator, we additionally bundle the keyframe stream into bounded submaps \mathcal{P}_ℓ^a (indexed by agent $a \in \mathcal{A}$ and per-agent submap counter $\ell = 1, \dots, L_a$; a second submap is denoted (b, m)), each holding its keyframes’ poses, depths, and Gaussians. A submap is frozen once it reaches K_{max} keyframes or the camera centers exceed a Euclidean distance of τ_{move} ; freezing detaches it from local bundle adjustment and assigns it a per-submap Sim(3) correction $C_\ell^a \in \text{Sim}(3)$ that maps the submap’s local coordinates into the aligned global frame, initialized to $C_\ell^a = \mathbf{I}$ and later refined jointly by the coordinator. Successive frozen submaps from the same agent are linked by a temporal Sim(3) edge $e \in \mathcal{E}^t$ of the global submap graph \mathcal{G}^{sm} (Section 3.2). The above chains anchor the looser inter-agent constraints.

3.2 Global Collaborative Pose Graph Optimization

The coordinator turns each agent’s frozen submaps into a global Sim(3) graph in four stages, including **encoding, retrieval, verification, joint optimization**, augmented by a reactive path that integrates PGBA corrections without re-running the front-end.

3.2.1 Compact submap summary. Raw keyframes and Gaussians are too large for inter-agent transmission, so each frozen submap is encoded as

$$\mathcal{S}_\ell^a = (\mathbf{d}_\ell^a, \mathcal{Q}_\ell^a, \mathcal{R}_\ell^a, [\mathbf{b}_{\min}, \mathbf{b}_{\max}]_\ell^a, \mathbf{A}_\ell^a), \quad (5)$$

where $\mathbf{d}_\ell^a \in \mathbb{R}^{128}$ is a mean-pooled DROID global descriptor, \mathcal{Q}_ℓ^a holds up to N_Q salient 3D points with local descriptors selected by the per-pixel score

$$\sigma(\mathbf{u}) = \|\nabla \mathbf{F}\|_{\mathbf{u}} + \lambda_d \|\nabla \mathbf{d}\|_{\mathbf{u}} + \lambda_F \|\mathbf{F}\|_{\mathbf{u}}, \quad (6)$$

with \mathbf{F} the per-pixel DROID feature; the three terms reward feature-edge strength, depth boundaries, and feature distinctiveness. \mathcal{R}_ℓ^a is a registration cloud for ICP [1], the bounding volume $[\mathbf{b}_{\min}, \mathbf{b}_{\max}]_\ell^a$

supplies the normalization scale of Eq. (10), and \mathbf{A}_ℓ^a packages the anchor keyframe (pose, image, disparity, intrinsics).

3.2.2 Retrieval and correspondence. Each new summary is matched against a top- K shortlist $\{\mathcal{S}_m^b\}$ by cosine similarity on \mathbf{d}_ℓ^a gated by τ_{sim} . For each candidate \mathcal{S}_m^b , a matcher $\Pi(\mathcal{S}_\ell^a, \mathcal{S}_m^b; \boldsymbol{\theta}_{\text{match}})$, including mutual nearest-neighbor matching jointly gated by an absolute cosine threshold, a best/second-best margin, and Lowe’s ratio test bundled into $\boldsymbol{\theta}_{\text{match}}$, returns a correspondence set \mathcal{M} with $|\mathcal{M}| \geq N_{\text{min}}$. When texture is sparse, dense LoFTR [42] matches between anchor images are back-projected and appended to the set.

3.2.3 Sim(3) estimation and verification cascade. A RANSAC loop estimates the relative Sim(3) transform $T^{t \leftarrow s}$ via Umeyama [47]:

$$\boldsymbol{\Gamma} = \frac{1}{N} \sum_i (\mathbf{p}_i^t - \bar{\mathbf{p}}^t)(\mathbf{p}_i^s - \bar{\mathbf{p}}^s)^\top, \quad \boldsymbol{\Gamma} = \mathbf{U}\boldsymbol{\Lambda}\mathbf{V}^\top, \quad (7)$$

$$\mathbf{R} = \mathbf{U}\mathbf{D}\mathbf{V}^\top, \quad s = \frac{\text{tr}(\mathbf{A}\mathbf{D})}{\sigma_s^2}, \quad \mathbf{t} = \bar{\mathbf{p}}^t - s\mathbf{R}\bar{\mathbf{p}}^s, \quad (8)$$

with $\boldsymbol{\Lambda}$ the diagonal of singular values of $\boldsymbol{\Gamma}$, \mathbf{D} handling reflections, and $\sigma_s^2 = \frac{1}{N} \sum_i \|\mathbf{p}_i^s - \bar{\mathbf{p}}^s\|^2$ the source-point variance. The surviving inlier set is denoted $\mathcal{X}_{\text{inl}} = \mathcal{X}_{\text{inl}}^s \cup \mathcal{X}_{\text{inl}}^t$, with $\mathcal{X}_{\text{inl}}^s$ and $\mathcal{X}_{\text{inl}}^t$ the matched 3D points in the source and target submap ($\mathcal{P}^s, \mathcal{P}^t$) respectively, and is then refined by ICP [1]. Rather than gating each candidate against a stack of independent thresholds, we collect all per-pair checks into a single verification predicate with the bundled gate thresholds $\boldsymbol{\theta}_V$,

$$V(s, \Phi, \rho_{\text{icp}}, \boldsymbol{\eta}; \boldsymbol{\theta}_V) \in \{0, 1\}, \quad (9)$$

which is true iff the recovered scale s lies in the monocular plausibility band, the ICP fitness Φ and RMSE ρ_{icp} clear their bounds, and the spatial-extent ratio

$$\eta = \min\left(\frac{\text{ext}(\mathcal{X}_{\text{inl}}^s)}{\text{diag}(\mathcal{P}^s)}, \frac{\text{ext}(\mathcal{X}_{\text{inl}}^t)}{\text{diag}(\mathcal{P}^t)}\right) \geq \tau_{\text{ext}}, \quad (10)$$

clears the gate; here $\text{ext}(\mathcal{X}) = \|\max \mathcal{X} - \min \mathcal{X}\|$ is the AABB diagonal of a point set and $\text{diag}(\mathcal{P}^{s/t}) = \|\mathbf{b}_{\text{max}}^{s/t} - \mathbf{b}_{\text{min}}^{s/t}\|$ reuses the submap bounding box from \mathcal{S} .

3.2.4 Pose graph optimization objective. The accepted constraints from §3.2.3 feed a Sim(3) submap pose graph $\mathcal{G}^{\text{sm}} = (\{\mathcal{P}_\ell^a\}, \mathcal{E}^{\text{sm}})$ with $\mathcal{E}^{\text{sm}} = \mathcal{E}^t \cup \mathcal{E}^v$ (intra-agent temporal and verified inter-agent edges), where the Sim(3) parameterization is used to accommodate the per-agent monocular scale ambiguity. We optimize the Sim(3) parameterization with the cost couples geometric residuals

$$\mathbf{r}_e^{\text{geo}} = \log(M_e^{-1} \circ C_{\text{tgt}}^{-1} \circ C_{\text{src}}) \in \mathbb{R}^7 \quad (11)$$

and anchor-image photometric residuals

$$\mathbf{r}_e^{\text{pho}}(\mathbf{u}) = I^{\text{src}}(\mathbf{u}) - I^{\text{tgt}}(\pi^{\text{tgt}}(C_{\text{tgt}}^{-1} \circ C_{\text{src}} \cdot \mathbf{p}^{\text{src}}(\mathbf{u}))), \quad (12)$$

where $M_e \in \text{Sim}(3)$ is the verified source to target relative transform on edge e , $C_{\text{src}}, C_{\text{tgt}}$ are the per-submap corrections of its endpoints, and $I^{\text{tgt}}(\cdot)$ denotes bilinear sampling of the target anchor image at sub-pixel coordinates. Jacobians w.r.t. $C_{\text{src}}, C_{\text{tgt}}$ follow by chain rule through this image sampler and π^{tgt} , as in standard direct alignment on Sim(3) [7, 8]. Here, the jointly geometric and photometric optimization objective is

$$\mathcal{L}^{\text{graph}}(\{C_\ell^a\}) = \sum_{e \in \mathcal{E}^{\text{sm}}} w_e \|\mathbf{r}_e^{\text{geo}}\|_\rho^2 + \sum_{e \in \mathcal{E}^v} \frac{w_e^{\text{pho}}}{|\mathcal{U}_e|} \|\mathbf{r}_e^{\text{pho}}\|_\rho^2, \quad (13)$$

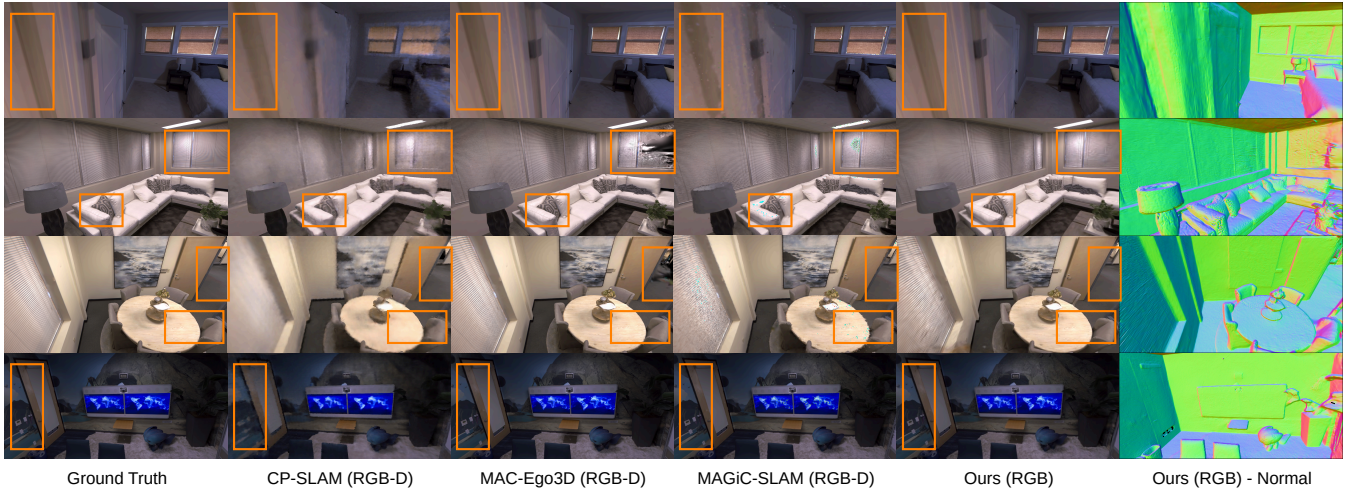


Figure 3: Qualitative comparison on the ReplicaMultiagent dataset. We visualize reconstruction and rendering results of MAGS-SLAM and competing multi-agent SLAM methods on representative Replica scenes. The comparison highlights differences in map completeness, photometric fidelity, and cross-agent consistency after global alignment and fusion.

Algorithm 1: Submap Graph Update

Input: summary \mathcal{S}_ℓ^a ; PGBA fit $(\Delta_{a,\ell}, \rho_{\text{rig}})$

Output: updated corrections $\{C_\ell^a\}$, fusable set \mathcal{F}

if \mathcal{S}_ℓ^a is new **then**

 add edge $\mathcal{S}_{\ell-1}^a \rightarrow \mathcal{S}_\ell^a$ to \mathcal{E}^t with weight w^t

foreach $\mathcal{S}_m^b \in \text{TopK}(\mathbf{d}_\ell^a; \tau_{\text{sim}})$ **do**

$\mathcal{M} \leftarrow \Pi(\mathcal{S}_\ell^a, \mathcal{S}_m^b; \theta_{\text{match}})$

$T^{t \leftarrow s}, \mathcal{X}_{\text{inl}} \leftarrow \text{Ransac-Umeyama}(\mathcal{M})$

$T^{t \leftarrow s} \leftarrow \text{ICP}(T^{t \leftarrow s}, \mathcal{R}_\ell^a, \mathcal{R}_m^b)$

if $V(\cdot; \theta_V)$ (Eq. (9)) **then** add edge $(T^{t \leftarrow s}, w^v)$ to \mathcal{E}^v

end

else

if $\rho_{\text{rig}} > \tau_{\text{rig}}$ **then**

 invalidate inter-agent edges incident to \mathcal{S}_ℓ^a

else

 update each M_e analytically (Eq. (14))

end

 drop photometric cache of \mathcal{S}_ℓ^a

end

$\{C_\ell^a\} \leftarrow \arg \min \mathcal{L}^{\text{graph}}$ (Eq. (13))

$\mathcal{F} \leftarrow \{(a, \ell) : \bar{\rho}_e(\mathcal{S}_\ell^a) \leq \tau_{\text{res}} \wedge |\mathcal{E}^v(\mathcal{S}_\ell^a)| \geq 1\}$

where $\{C_\ell^a\} = \{C_\ell^a : a \in \mathcal{A}, \ell = 1, \dots, L_a\}$ is the set of all per-submap corrections and \mathcal{U}_e is the in-frame, finite-depth anchor-pixel set of edge e ; the per-edge normalization makes inter-agent pairs of different overlap extents comparable. Edge weights split into intra-agent temporal w^t (on \mathcal{E}^t) and inter-agent w^v (on \mathcal{E}^v) with $w^t \gg w^v$, so trusted temporal chains anchor the looser inter-agent constraints; w_e^{pho} only fires on verified inter-agent edges. The graph is solved by damped Gauss-Newton within a Levenberg-Marquardt trust region [22, 30], with the first frozen submap fixed at identity. After convergence, only submaps whose mean per-edge

residual $\bar{\rho}_e(\mathcal{S}_\ell^a)$ falls below τ_{res} and that carry at least one inter-agent edge are forwarded to fusion (§3.3); the rest stay in the graph for re-evaluation as new evidence arrives.

3.2.5 Reactive update on PGBA. When an agent reports a PGBA correction $\Delta_{a,\ell} \in \text{Sim}(3)$ from Eq. (3) on submap \mathcal{P}_ℓ^a , we fit $\Delta_{a,\ell}$ by Umeyama on its pre/post-PGBA keyframe camera centers and take the alignment RMSE as the rigidity residual. If it exceeds τ_{rig} , all incident edges $e \in \mathcal{E}^v$ are invalidated and queued for re-verification; otherwise the bulk shift is rigid enough that we update each stored M_e analytically,

$$M_e \leftarrow \begin{cases} M_e \circ \Delta_{a,\ell}^{-1}, & a = \text{src}(e), \\ \Delta_{a,\ell} \circ M_e, & a = \text{tgt}(e). \end{cases} \quad (14)$$

Independently of which branch is taken, we drop the cached anchor-image photometric payload of \mathcal{P}_ℓ^a , since PGBA may have shifted its anchor pose and inverse depth even when the bulk drift is rigid; the payload is rebuilt lazily on the next evaluation of $\mathbf{r}_e^{\text{pho}}$.

3.3 Occupancy-Aware Asynchronous Fusion

After pose-graph convergence, each submap carries a $\text{Sim}(3)$ correction C_ℓ^a . Applying this correction to a Gaussian yields

$$\boldsymbol{\mu}'_i = s\mathbf{R}\boldsymbol{\mu}_i + \mathbf{t}, \quad \boldsymbol{\Sigma}'_i = s^2\mathbf{R}\boldsymbol{\Sigma}_i\mathbf{R}^\top, \quad s'_i = ss_i, \quad (15)$$

with unchanged opacity and color (quaternion rotation composed accordingly). The scale factor is critical for RGB-only operation. Fusion proceeds asynchronously per target agent using a frustum-aware occupancy grid of voxel size $v = 0.10\text{m}$. For the target map we precompute occupied voxels

$$\mathcal{O}_{\text{occ}} = \bigcup_{G_i \in \mathcal{G}^{\text{tgt}}} \{\kappa(\mathbf{x}) : \mathbf{x} \in [\boldsymbol{\mu}_i - ks_i, \boldsymbol{\mu}_i + ks_i]\} \quad (16)$$

and free-space voxels carved by ray-casting every keyframe depth map:

$$\mathcal{O}_{\text{free}} = \bigcup_{\mathbf{u}, k} \{\kappa(\mathbf{c}_k + t(\mathbf{r}_k(\mathbf{u}) - \mathbf{c}_k)) : t \in [0, 1)\}. \quad (17)$$

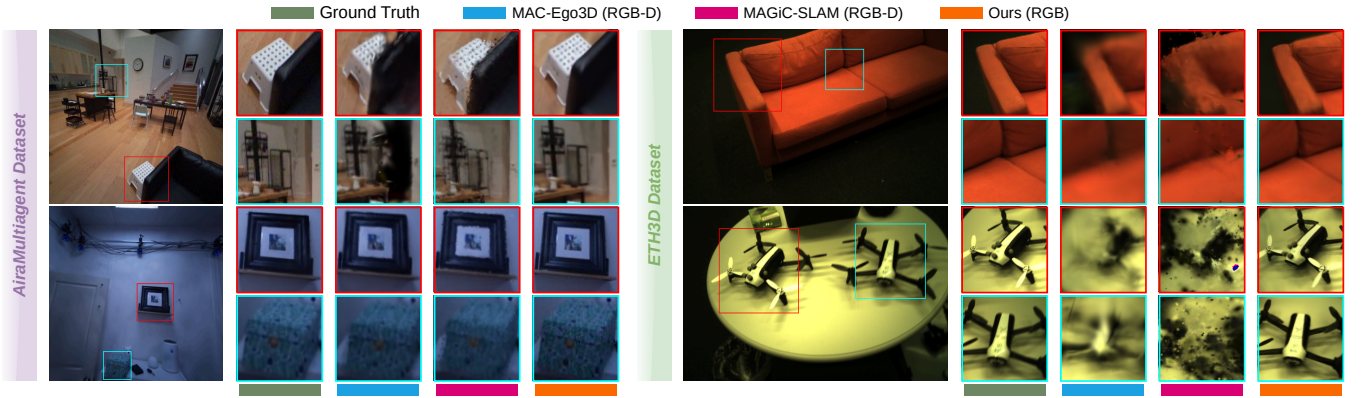


Figure 4: Qualitative comparison of multi-agent reconstruction on AiraMultiagent [31] dataset and ETH3D [39] dataset.

Table 1: Multi-agent tracking accuracy comparison (ATE RMSE [cm] ↓) on ReplicaMultiagent datasets. Best results are highlighted as first, second, and third. "-" indicates sequences without reported results in the original papers or unavailable code. "X" indicates invalid results due to the failure.

Method	Input	Office-0			Apartment-0			Apartment-1			Apartment-2		
		Agent 1	Agent 2	Avg.	Agent 1	Agent 2	Avg.	Agent 1	Agent 2	Avg.	Agent 1	Agent 2	Avg.
Swarm-SLAM [20]	RGB-D	1.07	1.76	1.42	1.61	1.98	1.80	4.62	6.50	5.56	2.69	8.53	5.61
CP-SLAM [12]	RGB-D	0.50	0.79	0.65	0.62	1.28	0.95	1.11	1.72	1.42	1.41	2.41	1.91
MNE-SLAM [6]	RGB-D	0.28	0.33	0.31	0.43	0.54	0.48	1.21	0.99	1.02	0.43	0.74	0.59
MCN-SLAM [5]	RGB-D	-	-	-	0.42	0.52	0.46	1.18	0.97	1.00	0.41	0.71	0.57
MAGiC-SLAM [53]	RGB-D	0.31	0.24	0.27	0.13	0.21	0.16	0.21	0.30	0.26	0.42	0.22	0.32
GRAND-SLAM [45]	RGB-D	0.28	0.25	0.26	0.27	0.19	0.23	0.28	0.36	0.32	0.18	0.18	0.18
CCM-SLAM [37]	RGB	9.84	0.76	5.30	X	X	X	2.12	9.31	5.71	0.51	0.48	0.49
MultiSlam-DiffPose [25]	RGB	0.41	0.75	0.58	0.68	0.25	0.47	0.63	0.68	0.65	0.32	0.40	0.36
MA-MASt3R-SLAM [58]	RGB	3.79	1.34	2.57	3.27	7.20	5.24	4.60	6.35	5.48	-	-	-
MAGS-SLAM (Ours)	RGB	0.47	0.12	0.29	0.50	0.42	0.46	0.59	0.34	0.46	0.29	0.34	0.31

Table 2: Multi-agent tracking accuracy comparison (ATE RMSE [cm] ↓) on real-world AriaMultiagent datasets. Best results are highlighted as first, second, and third. "-" indicates that CP-SLAM does not support settings with more than two agent. "X" indicates invalid results due to the failure.

Method	Input	Room-0				Room-1			
		Ag.1	Ag.2	Ag.3	Avg.	Ag.1	Ag.2	Ag.3	Avg.
Swarm-SLAM	RGB-D	6.11	8.43	4.82	6.45	4.29	4.95	5.12	4.78
CP-SLAM	RGB-D	0.68	8.43	-	3.03	5.06	0.68	-	2.87
MNE-SLAM	RGB-D	1.93	2.52	0.98	1.81	1.24	0.72	0.91	0.95
MAGiC-SLAM	RGB-D	0.67	1.13	1.67	1.15	0.96	0.53	0.46	0.65
CCM-SLAM	RGB	X	X	X	X	X	X	X	X
MultiSlam-DiffPose	RGB	1.07	1.30	0.79	1.05	0.84	0.60	1.11	0.85
Ours	RGB	1.02	1.04	0.51	0.86	0.83	0.52	0.26	0.54

A borrowed Gaussian G_j is retained only if

$$\kappa(\mu_j) \notin \mathcal{O}_{\text{occ}} \text{ and } \kappa(\mu_j) \notin \mathcal{O}_{\text{free}}. \quad (18)$$

The occupied test suppresses duplicate Gaussians, while the free-space test prevents inserting source primitives into regions already observed as empty by the target agent. We pack each voxel index $\kappa(\cdot)$ into a 64-bit spatial-hash key, reducing the membership tests in Eq. (18) to constant-time lookups. After deduplication, small

residual $\text{Sim}(3)$ errors and exposure differences are resolved by joint photometric refinement of the fused Gaussian set $\mathcal{G}^{\text{fused}} = \mathcal{G}^{\text{tgt}} \cup \{G_j : \text{Eq. (18)}\}$, per-keyframe pose deltas δ_{ξ_k} , and per-keyframe log-gain and bias $(a_k, b_k) \in \mathbb{R}^2$, with $\tilde{I}(\mathbf{u}) = e^{a_k} \hat{I}(\mathbf{u}) + b_k$ and \hat{I}, \hat{D} the differentially rendered RGB and depth of $\mathcal{G}^{\text{fused}}$. The refinement loss reuses the photometric, depth, and normal terms of Eq. (4) but evaluates them on the exposure-compensated render \tilde{I} , and adds a structural-similarity term:

$$\mathcal{L}^{\text{refine}} = \alpha' \mathcal{L}_1(\tilde{I}, I) + \lambda(1 - \text{SSIM}(\tilde{I}, I)) + \beta \mathcal{L}_1(\hat{D}, \bar{D}) + \lambda'_n \mathcal{L}^{\text{normal}}, \quad (19)$$

with $\alpha' = (1 - \lambda) + \alpha = 1.75$, $\lambda = 0.2$, β inherited from Eq. (4), and $\lambda'_n = 10$, $\lambda_n = 0.1$ raised to anchor geometry against photometric drift. \bar{D} is derived from the scaled D . The refinement runs for 2,000 iterations at half the per-agent learning rate and prunes Gaussians with opacity below 0.005, producing a globally consistent map.

4 Analysis

4.1 Tracking Accuracy and Localization

As the first RGB-only multi-agent 3D Gaussian Splatting SLAM system based on monocular input, MAGS-SLAM achieves highly competitive trajectory estimation under pure monocular input. Table 1 reports Absolute Trajectory Error (ATE) RMSE [cm] on the ReplicaMultiagent benchmark. Despite without depth information, our

Table 3: Multi-agent rendering quality comparison (PSNR/SSIM/LPIPS $\uparrow\downarrow$) on ReplicaMultiagent datasets. Best results are highlighted as first, second, and third.

Method	Input	Office-0			Apartment-0			Apartment-1			Apartment-2		
		PSNR \uparrow	SSIM \uparrow	LPIPS \downarrow	PSNR \uparrow	SSIM \uparrow	LPIPS \downarrow	PSNR \uparrow	SSIM \uparrow	LPIPS \downarrow	PSNR \uparrow	SSIM \uparrow	LPIPS \downarrow
CP-SLAM [12]	RGB-D	32.61	0.90	0.29	32.16	0.91	0.23	27.42	0.78	0.36	25.12	0.77	0.37
MNE-SLAM [6]	RGB-D	28.27	0.86	0.08	27.46	0.87	0.27	25.45	0.73	0.41	26.16	0.81	0.31
MAGiC-SLAM [53]	RGB-D	39.32	0.99	0.05	36.96	0.98	0.09	30.01	0.95	0.18	30.73	0.96	0.17
HAMMER [52]	RGB-D	43.02	0.98	0.04	40.89	0.97	0.06	31.43	0.90	0.13	33.78	0.94	0.11
GRAND-SLAM [45]	RGB-D	43.12	0.99	0.03	44.15	0.99	0.03	38.65	0.99	0.05	39.46	0.99	0.06
MAC-Ego3D [49]	RGB-D	42.43	0.98	0.03	42.83	0.98	0.05	36.28	0.97	0.06	38.59	0.98	0.06
CoMA-SLAM [4]	RGB-D	42.77	1.00	0.02	42.28	0.99	0.03	33.86	0.98	0.08	34.59	0.98	0.08
MAGS-SLAM (Ours)	RGB	43.24	0.99	0.02	42.83	0.99	0.02	36.28	0.96	0.06	38.99	0.98	0.04

Table 4: Multi-agent rendering quality comparison (PSNR/SSIM/LPIPS $\uparrow\downarrow$) on real-world AriaMultiagent datasets. Best results are highlighted as first, second, and third.

Method	Input	Room-0			Room-1		
		PSNR \uparrow	SSIM \uparrow	LPIPS \downarrow	PSNR \uparrow	SSIM \uparrow	LPIPS \downarrow
CP-SLAM	RGB-D	8.96	0.32	0.91	9.17	0.24	0.95
MNE-SLAM	RGB-D	19.23	0.78	0.39	22.02	0.84	0.27
MAGiC-SLAM	RGB-D	23.45	0.89	0.22	21.78	0.85	0.21
MAC-Ego3D	RGB-D	22.85	0.81	0.36	28.17	0.91	0.20
CoMA-SLAM	RGB-D	25.41	0.90	0.21	21.80	0.85	0.20
Ours	RGB	29.03	0.92	0.19	31.02	0.95	0.11

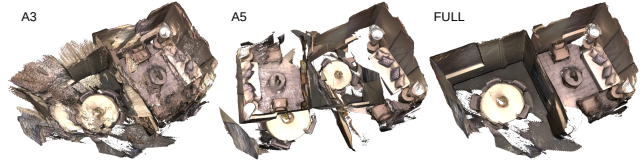
Table 5: Multi-agent rendering quality comparison (PSNR/SSIM/LPIPS $\uparrow\downarrow$) on real-world ETH3D datasets. Best results are highlighted as first, second, and third.

Method	Metric	Sofa	Table	Plant-Scene	Mannequin	Planar
CP-SLAM	PSNR \uparrow	25.28	15.44	20.10	18.76	16.74
	SSIM \uparrow	0.819	0.522	0.654	0.598	0.431
	LPIPS \downarrow	0.330	0.621	0.499	0.605	0.706
MNE-SLAM	PSNR \uparrow	22.30	19.48	22.72	24.35	15.18
	SSIM \uparrow	0.747	0.672	0.746	0.757	0.318
	LPIPS \downarrow	0.424	0.493	0.399	0.486	0.846
MAGiC-SLAM	PSNR \uparrow	25.25	18.42	24.62	23.68	17.35
	SSIM \uparrow	0.799	0.680	0.849	0.784	0.588
	LPIPS \downarrow	0.496	0.491	0.352	0.477	0.542
MAC-Ego3D	PSNR \uparrow	27.09	20.46	26.02	27.20	17.04
	SSIM \uparrow	0.926	0.851	0.931	0.929	0.621
	LPIPS \downarrow	0.178	0.218	0.139	0.144	0.569
Ours	PSNR \uparrow	30.67	27.05	31.32	31.99	22.68
	SSIM \uparrow	0.953	0.938	0.961	0.939	0.864
	LPIPS \downarrow	0.138	0.154	0.108	0.191	0.222

method matches or outperforms several RGB-D baselines and substantially surpasses previous RGB-only approaches, such as CCM-SLAM [37], MultiSLAM-DiffPose [25] and MA-MAS3R-SLAM [58]. Similar trends hold on the real-world AriaMultiagent dataset (Table 2), where MAGS-SLAM maintains robust multi-agent alignment even under challenging real-world indoor environment. Notably, on Room-0 and Room-1 sequences, MAGS-SLAM attains average errors of 0.86 cm and 0.54 cm respectively, which are on par with or better than the RGB-D state-of-the-art methods MNE-SLAM [6] and MAGiC-SLAM [53].

Table 6: Ablation Studies on ReplicaMultiagent Dataset. Details about each configuration are described in §4.3.

Method	PSNR \uparrow	SSIM \uparrow	LPIPS \downarrow
A1. w/o sim(3)-PGBA update	36.32	0.963	0.057
A2. w/o photometric residuals	37.88	0.967	0.045
A3. w/o occupancy-aware fusion	33.16	0.941	0.113
A4. w/o pose-Gaussian joint refinement	38.94	0.974	0.041
A5. w/o scale estimation, i.e., SE(3)	18.61	0.718	0.390
Full	40.33	0.981	0.035

**Figure 5: Qualitative ablation on Apart-2 from ReplicaMultiagent Dataset. A3 (w/o occupancy-aware fusion) produces double-shells and ghosted geometry on shared surfaces; A5 (w/o scale estimation, i.e., SE(3)) fuses the second agent at the wrong metric scale, tearing the scene apart; Full yields a clean, consistent reconstruction.**

4.2 Photorealistic Mapping and Novel View Synthesis

Tables 7, 4, and 5 report rendering quality on ReplicaMultiagent, AriaMultiagent, and ETH3D. Despite using only RGB input, MAGS-SLAM attains the best PSNR, SSIM, and LPIPS across all three benchmarks. On ReplicaMultiagent it reaches 43.24/42.83/38.99 dB PSNR on Office-0, Apartment-0, and Apartment-2, surpassing RGB-D baselines such as MAGiC-SLAM [53], MAC-Ego3D [49], and CoMA-SLAM [4]. On the real-world AriaMultiagent sequences, it achieves 29.03 and 31.02 dB on Room-0 and Room-1, exceeding the strongest RGB-D competitor by 3.6 and 2.9 dB. On the more challenging ETH3D multi-agent benchmark it ranks first on all five scenes, with 3-7 dB PSNR gains over MAC-Ego3D. Qualitative comparisons (Fig. 3 and 4) confirm these gains: our occupancy-aware fusion and joint pose-Gaussian refinement yield seamless reconstructions free of ghosting seams, while MAGiC-SLAM and MAC-Ego3D show misalignment and duplicated Gaussians at agent boundaries that the frustum-aware occupancy grid and final refinement together eliminate.

4.3 Ablation Study

Table 6 ablates each design component on ReplicaMultiagent by disabling one at a time; every variant degrades all three metrics. Removing the Sim(3)-PGBA update, which propagates the verified inter-agent Sim(3) back into per-agent keyframes rather than only the submap node, costs 4.0 dB, as residual intra-submap scale drift is left for the rasteriser to absorb. Replacing the photometric inter-agent residual with a purely geometric one drops PSNR to 37.88 dB: the photometric term tightens the relative Sim(3) on textured but geometrically ambiguous overlaps such as wall-floor seams. Disabling the frustum-aware occupancy grid in favour of naive Gaussian-centre deduplication is the second-largest hit, since slightly mis-aligned per-agent populations form double-shells on shared surfaces. Skipping the joint pose-Gaussian refinement costs only 1.4 dB but supplies the sub-voxel correction needed for sharp rendering. Finally, replacing the Sim(3) graph with a rigid SE(3) one collapses PSNR to 18.61 dB and inflates LPIPS by an order of magnitude, confirming that explicit scale estimation is mandatory in the multi-agent monocular regime where per-agent maps live at incompatible metric scales.

5 Conclusion

We propose MAGS-SLAM, the first monocular RGB-only multi-agent 3D Gaussian Splatting SLAM system. By combining a monocular front-end with compact submap summaries, a PGBA-consistent Sim(3) pose graph augmented by geometric and photometric residuals and a spatial-extent gate, adaptive edge invalidation, and an occupancy-aware asynchronous fusion framework, our method achieves globally consistent collaborative reconstruction from purely monocular video. On ReplicaMultiagent, AriaMultiagent, ETH3D, and our ReplicaMultiagent Plus (supplementary materials), MAGS-SLAM achieves competitive tracking accuracy and comparable or superior rendering quality to state-of-the-art RGB-D collaborative Gaussian SLAM methods without requiring any depth sensors.

Although MAGS-SLAM already enables practical photorealistic collaboration with ubiquitous RGB cameras, scaling the approach to ultra-large environments remains an open frontier. Future work will explore more efficient global map management, and tighter integration with large foundation models for even more robust scale recovery and semantic understanding. These advancements will unlock transformative applications in immersive telepresence, virtual production, and large-scale digital twins.

References

- [1] Paul J Besl and Neil D McKay. 1992. Method for registration of 3-D shapes. In *Sensor fusion IV: control paradigms and data structures*, Vol. 1611. Spie, 586–606.
- [2] Carlos Campos, Richard Elvira, Juan J Gómez Rodríguez, José MM Montiel, and Juan D Tardós. 2021. Orb-slam3: An accurate open-source library for visual, visual-inertial, and multimap slam. *IEEE transactions on robotics* 37, 6 (2021), 1874–1890.
- [3] Zhihao Cao, Hanyu Wu, Li Wa Tang, Zizhou Luo, Wei Zhang, Marc Pollefeys, Zihan Zhu, and Martin R Oswald. 2025. Mcgs-slam: A multi-camera slam framework using gaussian splatting for high-fidelity mapping. *arXiv preprint arXiv:2509.14191* (2025).
- [4] Lin Chen, Yongxin Su, Jvboxi Wang, Pengcheng Han, Zhenyu Xia, Shuhui Bu, Kun Li, Boni Hu, Shengqi Meng, and Guangming Wang. 2026. CoMA-SLAM: Collaborative Multi-Agent Gaussian SLAM with Geometric Consistency. In *Proceedings of the AAAI Conference on Artificial Intelligence*, Vol. 40. 2922–2929.
- [5] Tianchen Deng, Guole Shen, Xun Chen, Shenghai Yuan, Hongming Shen, Guohao Peng, Zhenyu Wu, Jingchuan Wang, Lihua Xie, Danwei Wang, et al. 2025. Mcn-slam: Multi-agent collaborative neural slam with hybrid implicit neural scene representation. *arXiv preprint arXiv:2506.18678* (2025).
- [6] Tianchen Deng, Guole Shen, Chen Xun, Shenghai Yuan, Tongxin Jin, Hongming Shen, Yanbo Wang, Jingchuan Wang, Hesheng Wang, Danwei Wang, et al. 2025. Mcn-slam: Multi-agent neural slam for mobile robots. In *Proceedings of the Computer Vision and Pattern Recognition Conference*. 1485–1494.
- [7] Jakob Engel, Vladlen Koltun, and Daniel Cremers. 2017. Direct sparse odometry. *IEEE transactions on pattern analysis and machine intelligence* 40, 3 (2017), 611–625.
- [8] Jakob Engel, Thomas Schöps, and Daniel Cremers. 2014. LSD-SLAM: Large-scale direct monocular SLAM. In *European conference on computer vision*. Springer, 834–849.
- [9] Ben Glocker, Shahram Izadi, Jamie Shotton, and Antonio Criminisi. 2013. Real-time RGB-D camera relocalization. In *2013 IEEE International Symposium on Mixed and Augmented Reality (ISMAR)*. IEEE, 173–179.
- [10] Seongbo Ha, Jiung Yeon, and Hyeonwoo Yu. 2024. Rgbd gs-icp slam. In *European conference on computer vision*. Springer, 180–197.
- [11] Jiarui Hu, Xianhao Chen, Boyin Feng, Guanglin Li, Liangjing Yang, Hujun Bao, Guofeng Zhang, and Zhaopeng Cui. 2024. Cg-slam: Efficient dense rgb-d slam in a consistent uncertainty-aware 3d gaussian field. In *European Conference on Computer Vision*. Springer, 93–112.
- [12] Jiarui Hu, Mao Mao, Hujun Bao, Guofeng Zhang, and Zhaopeng Cui. 2023. Cp-slam: Collaborative neural point-based slam system. *Advances in Neural Information Processing Systems* 36 (2023), 39429–39442.
- [13] Mu Hu, Wei Yin, Chi Zhang, Zhipeng Cai, Xiaoxiao Long, Hao Chen, Kaixuan Wang, Gang Yu, Chunhua Shen, and Shaojie Shen. 2024. Metric3d v2: A versatile monocular geometric foundation model for zero-shot metric depth and surface normal estimation. *IEEE Transactions on Pattern Analysis and Machine Intelligence* 46, 12 (2024), 10579–10596.
- [14] Binbin Huang, Zehao Yu, Anpei Chen, Andreas Geiger, and Shenghua Gao. 2024. 2d gaussian splatting for geometrically accurate radiance fields. In *ACM SIGGRAPH 2024 conference papers*. 1–11.
- [15] Huajian Huang, Longwei Li, Hui Cheng, and Sai-Kit Yeung. 2024. Photo-slam: Real-time simultaneous localization and photorealistic mapping for monocular stereo and rgb-d cameras. In *Proceedings of the IEEE/CVF Conference on Computer Vision and Pattern Recognition*. 21584–21593.
- [16] Mohammad Mahdi Johari, Camilla Carta, and François Fleuret. 2023. Eslam: Efficient dense slam system based on hybrid representation of signed distance fields. In *Proceedings of the IEEE/CVF conference on computer vision and pattern recognition*. 17408–17419.
- [17] Nikhil Keetha, Jay Karhade, Krishna Murthy Jatavallabhula, Gengshan Yang, Sebastian Scherer, Deva Ramanan, and Jonathon Luiten. 2024. Splatam: Splat track & map 3d gaussians for dense rgb-d slam. In *Proceedings of the IEEE/CVF conference on computer vision and pattern recognition*. 21357–21366.
- [18] Bernhard Kerbl, Georgios Kopanas, Thomas Leimkühler, George Drettakis, et al. 2023. 3d gaussian splatting for real-time radiance field rendering. *ACM Trans. Graph.* 42, 4 (2023), 139–1.
- [19] Arno Knapitsch, Jaesik Park, Qian-Yi Zhou, and Vladlen Koltun. 2017. Tanks and temples: Benchmarking large-scale scene reconstruction. *ACM Transactions on Graphics (ToG)* 36, 4 (2017), 1–13.
- [20] Pierre-Yves Lajoie and Giovanni Beltrame. 2023. Swarm-slam: Sparse decentralized collaborative simultaneous localization and mapping framework for multi-robot systems. *IEEE Robotics and Automation Letters* 9, 1 (2023), 475–482.
- [21] Pierre-Yves Lajoie, Benjamin Ramtola, Yun Chang, Luca Carlone, and Giovanni Beltrame. 2020. DOOR-SLAM: Distributed, online, and outlier resilient SLAM for robotic teams. *IEEE Robotics and Automation Letters* 5, 2 (2020), 1656–1663.
- [22] Kenneth Levenberg. 1944. A method for the solution of certain non-linear problems in least squares. *Quarterly of applied mathematics* 2, 2 (1944), 164–168.
- [23] Mingrui Li, Shuhong Liu, Heng Zhou, Guohao Zhu, Na Cheng, Tianchen Deng, and Hongyu Wang. 2024. Sgs-slam: Semantic gaussian splatting for neural dense slam. In *European Conference on Computer Vision*. Springer, 163–179.
- [24] Yonghao Li, Ping Ye, and Qingxuan Jia. 2025. MANG-SLAM: Multi-Agent Neural Submap and Gaussian Representation for Dense Mapping. *IEEE Robotics and Automation Letters* 11, 2 (2025), 2242–2249.
- [25] Lahav Lipson and Jia Deng. 2024. Multi-session slam with differentiable wide-baseline pose optimization. In *Proceedings of the IEEE/CVF Conference on Computer Vision and Pattern Recognition*. 19626–19635.
- [26] Lorenzo Liso, Erik Sandström, Vladimir Yugay, Luc Van Gool, and Martin R Oswald. 2024. Loopy-slam: Dense neural slam with loop closures. In *Proceedings of the IEEE/CVF conference on computer vision and pattern recognition*. 20363–20373.
- [27] Hidenobu Matsuki, Riku Murai, Paul HJ Kelly, and Andrew J Davison. 2024. Gaussian splatting slam. In *Proceedings of the IEEE/CVF conference on computer vision and pattern recognition*. 18039–18048.
- [28] Riku Murai, Eric Dexeheimer, and Andrew J Davison. 2025. Mast3r-slam: Real-time dense slam with 3d reconstruction priors. In *Proceedings of the Computer Vision and Pattern Recognition Conference*. 16695–16705.
- [29] Richard A Newcombe, Steven J Lovegrove, and Andrew J Davison. 2011. DTAM: Dense tracking and mapping in real-time. In *2011 international conference on*

- computer vision. IEEE, 2320–2327.
- [30] Jorge Nocedal and Stephen J Wright. 2006. *Numerical optimization*. Springer.
- [31] Xiaqing Pan, Nicholas Charron, Yongqiang Yang, Scott Peters, Thomas Whelan, Chen Kong, Omkar Parkhi, Richard Newcombe, and Yuheng Carl Ren. 2023. Aria digital twin: A new benchmark dataset for egocentric 3d machine perception. In *Proceedings of the IEEE/CVF International Conference on Computer Vision*. 20133–20143.
- [32] Zhexi Peng, Tianjia Shao, Yong Liu, Jingke Zhou, Yin Yang, Jingdong Wang, and Kun Zhou. 2024. Rtg-slam: Real-time 3d reconstruction at scale using gaussian splatting. In *ACM SIGGRAPH 2024 conference papers*. 1–11.
- [33] Xavier Puig, Eric Undersander, Andrew Szot, Mikael Dalalre Cote, Tsung-Yen Yang, Ruslan Partsey, Ruta Desai, Alexander Clegg, Michal Hlavac, So Yeon Min, et al. 2024. Habitat 3.0: A co-habitat for humans, avatars, and robots. In *International Conference on Learning Representations*, Vol. 2024. 15306–15336.
- [34] Antoni Rosinol, John J Leonard, and Luca Carlone. 2023. Nerf-slam: Real-time dense monocular slam with neural radiance fields. In *2023 IEEE/RSJ International Conference on Intelligent Robots and Systems (IROS)*. IEEE, 3437–3444.
- [35] Erik Sandström, Yue Li, Luc Van Gool, and Martin R Oswald. 2023. Point-slam: Dense neural point cloud-based slam. In *Proceedings of the IEEE/CVF international conference on computer vision*. 18433–18444.
- [36] Erik Sandström, Ganlin Zhang, Keisuke Tateno, Michael Oechsle, Michael Niemeyer, Youmin Zhang, Manthan Patel, Luc Van Gool, Martin Oswald, and Federico Tombari. 2025. Splat-slam: Globally optimized rgb-only slam with 3d gaussians. In *Proceedings of the Computer Vision and Pattern Recognition Conference*. 1680–1691.
- [37] Patrik Schmuck and Margarita Chli. 2019. CCM-SLAM: Robust and efficient centralized collaborative monocular simultaneous localization and mapping for robotic teams. *Journal of Field Robotics* 36, 4 (2019), 763–781.
- [38] Patrik Schmuck, Thomas Ziegler, Marco Karrer, Jonathan Perraudin, and Margarita Chli. 2021. Covins: Visual-inertial slam for centralized collaboration. *arXiv preprint arXiv:2108.05756* (2021).
- [39] Thomas Schops, Torsten Sattler, and Marc Pollefeys. 2019. Bad slam: Bundle adjusted direct rgb-d slam. In *Proceedings of the IEEE/CVF Conference on Computer Vision and Pattern Recognition*. 134–144.
- [40] Julian Straub, Thomas Whelan, Lingni Ma, Yufan Chen, Erik Wijmans, Simon Green, Jakob J Engel, Raul Mur-Artal, Carl Ren, Shobhit Verma, et al. 2019. The replica dataset: A digital replica of indoor spaces. *arXiv preprint arXiv:1906.05797* (2019).
- [41] Edgar Sucar, Shikun Liu, Joseph Ortiz, and Andrew J Davison. 2021. imap: Implicit mapping and positioning in real-time. In *Proceedings of the IEEE/CVF international conference on computer vision*. 6229–6238.
- [42] Jiaming Sun, Zehong Shen, Yuang Wang, Hujun Bao, and Xiaowei Zhou. 2021. LoFTR: Detector-free local feature matching with transformers. In *Proceedings of the IEEE/CVF conference on computer vision and pattern recognition*. 8922–8931.
- [43] Zachary Teed and Jia Deng. 2021. Droid-slam: Deep visual slam for monocular, stereo, and rgb-d cameras. *Advances in neural information processing systems* 34 (2021), 16558–16569.
- [44] Zachary Teed, Lahav Lipson, and Jia Deng. 2023. Deep patch visual odometry. *Advances in Neural Information Processing Systems* 36 (2023), 39033–39051.
- [45] Annika Thomas, Aneesa Sonawalla, Alex Rose, and Jonathan P How. 2025. GRAND-SLAM: Local Optimization for Globally Consistent Large-Scale Multi-Agent Gaussian SLAM. *IEEE Robotics and Automation Letters* (2025).
- [46] Yulun Tian, Yun Chang, Fernando Herrera Arias, Carlos Nieto-Granda, Jonathan P How, and Luca Carlone. 2022. Kimera-multi: Robust, distributed, dense metric-semantic slam for multi-robot systems. *IEEE transactions on robotics* 38, 4 (2022).
- [47] Shinji Umeyama. 1991. Least-squares estimation of transformation parameters between two point patterns. *IEEE Transactions on pattern analysis and machine intelligence* 13, 4 (1991), 376–380.
- [48] Hengyi Wang, Jingwen Wang, and Lourdes Agapito. 2023. Co-slam: Joint coordinate and sparse parametric encodings for neural real-time slam. In *Proceedings of the IEEE/CVF conference on computer vision and pattern recognition*. 13293–13302.
- [49] Xiaohao Xu, Feng Xue, Shibo Zhao, Yike Pan, Sebastian Scherer, and Xiaonan Huang. 2025. Mac-ego3d: Multi-agent gaussian consensus for real-time collaborative ego-motion and photorealistic 3d reconstruction. In *Proceedings of the Computer Vision and Pattern Recognition Conference*. 854–863.
- [50] Chi Yan, Delin Qu, Dan Xu, Bin Zhao, Zhigang Wang, Dong Wang, and Xuelong Li. 2024. Gs-slam: Dense visual slam with 3d gaussian splatting. In *Proceedings of the IEEE/CVF conference on computer vision and pattern recognition*. 19595–19604.
- [51] Xingrui Yang, Hai Li, Hongjia Zhai, Yuhang Ming, Yuqian Liu, and Guofeng Zhang. 2022. Vox-fusion: Dense tracking and mapping with voxel-based neural implicit representation. In *2022 IEEE International Symposium on Mixed and Augmented Reality (ISMAR)*. IEEE, 499–507.
- [52] Javier Yu, Timothy Chen, and Mac Schwager. 2025. Hammer: heterogeneous, multi-robot semantic gaussian splatting. *IEEE Robotics and Automation Letters* (2025).
- [53] Vladimir Yugay, Theo Gevers, and Martin R Oswald. 2025. Magic-slam: Multi-agent gaussian globally consistent slam. In *Proceedings of the Computer Vision and Pattern Recognition Conference*. 6741–6750.
- [54] Vladimir Yugay, Yue Li, Theo Gevers, and Martin R Oswald. 2023. Gaussian-slam: Photo-realistic dense slam with gaussian splatting. *arXiv preprint arXiv:2312.10070* (2023).
- [55] Wei Zhang, Qing Cheng, David Skuddis, Niclas Zeller, Daniel Cremers, and Norbert Haala. 2025. Hi-slam2: Geometry-aware gaussian slam for fast monocular scene reconstruction. *IEEE Transactions on Robotics* 41 (2025), 6478–6493.
- [56] Wei Zhang, Tiecheng Sun, Sen Wang, Qing Cheng, and Norbert Haala. 2023. Hi-slam: Monocular real-time dense mapping with hybrid implicit fields. *IEEE Robotics and Automation Letters* 9, 2 (2023), 1548–1555.
- [57] Youmin Zhang, Fabio Tosi, Stefano Mattoccia, and Matteo Poggi. 2023. Go-slam: Global optimization for consistent 3d instant reconstruction. *Proceedings of the IEEE/CVF international conference on computer vision*. 3727–3737.
- [58] Yuchen Zhou and Haihang Wu. 2025. Multi-Agent Monocular Dense SLAM With 3D Reconstruction Priors. *arXiv preprint arXiv:2511.19031* (2025).
- [59] Liyuan Zhu, Yue Li, Erik Sandström, Shengyu Huang, Konrad Schindler, and Iro Armeni. 2025. Loopsplat: Loop closure by registering 3d gaussian splats. In *2025 International Conference on 3D Vision (3DV)*. IEEE, 156–167.
- [60] Zihan Zhu, Songyou Peng, Viktor Larsson, Zhaopeng Cui, Martin R Oswald, Andreas Geiger, and Marc Pollefeys. 2024. Nicer-slam: Neural implicit scene encoding for rgb slam. In *2024 International Conference on 3D Vision (3DV)*. IEEE, 42–52.
- [61] Zihan Zhu, Songyou Peng, Viktor Larsson, Weiwei Xu, Hujun Bao, Zhaopeng Cui, Martin R Oswald, and Marc Pollefeys. 2022. Nice-slam: Neural implicit scalable encoding for slam. In *Proceedings of the IEEE/CVF conference on computer vision and pattern recognition*. 12786–12796.
- [62] Zihan Zhu, Wei Zhang, Moyang Li, Norbert Haala, Marc Pollefeys, and Daniel Barath. 2025. Vigs-slam: visual inertial Gaussian splatting slam. *arXiv preprint arXiv:2512.02293* (2025).

A The ReplicaMultiagent Plus Benchmark

Existing multi-agent SLAM benchmarks force a trade-off between photometric realism, agent count, and ground-truth completeness. Real-world sets such as AriaMultiagent [31, 53], the multi-agent split of ETH3D [39], and the MNE/MCN-SLAM dataset [5, 6] provide authentic sensor noise but no dense mesh ground truth, no semantic supervision, and a fixed trajectory partition that cannot be re-configured. Synthetic sets built on Replica [12, 40] provide complete geometry but cap the agent count at two. Microsoft 7-Scenes [9], adopted as a multi-agent benchmark by treating its repeated recordings as independent agents, contributes real-world variability but ships only per-frame depth without a globally consistent mesh.

We address these gaps by re-rendering Replica scenes through the Habitat-Sim platform with up to four programmatically generated agent trajectories per scene. This produces a benchmark that simultaneously exposes (i) Replica’s native semantic labels, (ii) dense ground-truth depth and mesh from the simulator, (iii) configurable trajectory overlap between agents, and (iv) more than two simultaneous agents, while preserving the photometric fidelity. It will support the evaluation of monocular, RGB-D, and semantic multi-agent SLAM for collaborative dense reconstruction. It will support the evaluation of monocular, RGB-D, and semantic multi-agent SLAM for collaborative dense reconstruction.

A.1 Construction

A.1.1 Trajectory generation. For 6 of the Replica scenes we instantiate $N_a \in \{2, 3, 4\}$ embodied agents inside Habitat-Sim [33]. Their start poses are drawn from the simulator’s navigation mesh and then manually filtered so that the N_a seeds fall in distinct rooms or hallway segments; this lets us tune inter-agent overlap from largely disjoint to heavily co-visible without re-rolling the renderer. Rather than a purely procedural random walk, each trajectory is captured by a human operator teleoperating the agent at 30Hz with an Xbox

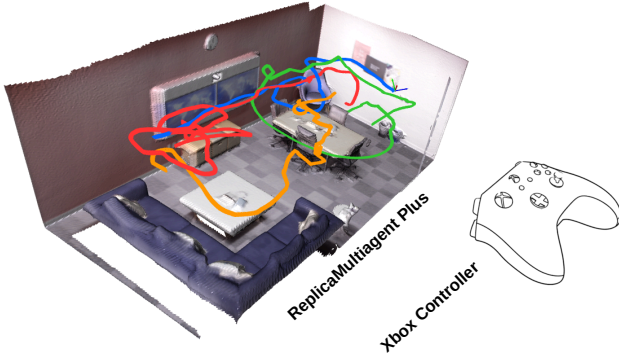


Figure 6: Xbox-controller mapping used for trajectory recording. The left analog stick drives planar translation in the agent’s local frame (forward/back, strafe); the right analog stick controls view orientation (yaw/pitch); the analog triggers LT/RT translate the agent vertically so the operator can clear thin obstacles or step onto raised surfaces. The A button toggles recording on/off and B ends the session. Synchronized RGB, depth, and semantic frames together with the (t, p, q) pose are written at 30Hz while recording is enabled.

controller: the left analog stick drives planar translation, the right stick controls yaw and pitch, and the analog triggers (LT/RT) translate the body vertically so the operator can clear thin obstacles or step onto raised surfaces. The operator is asked to cover the navigable area while loosely respecting a target overlap budget per scene, which yields motion that mixes long forward sweeps, lookarounds, brief stops, and occasional revisits of the same region. The full (t, p, q) pose is logged in TUM format alongside the frames, so the same trajectory can be deterministically re-rendered later at a different resolution or sensor set without re-recording.

A.1.2 Rendered modalities. Each agent carries a rigidly co-located RGB, depth, and semantic camera with an HFOV of 90° , and frames are rendered at 1200×680 at 30Hz. For every keyframe we export an 8-bit RGB image, dense metric depth stored as a 16-bit PNG in millimetres, surface normals, the per-pixel Replica semantic class id, and the camera pose in a common world frame. Pinhole intrinsics (f_x, f_y, c_x, c_y) are derived from the configured HFOV and shipped once per agent, so all N_a agents share the same camera model.

A.1.3 Sequence statistics. The released split contains 6 Replica scenes (OFFICE-2, APARTMENT-0, APARTMENT-2, OFFICE-2, ROOM-0, and FRL APARTMENT-3) with 4 agents each, $\sim 1,500$ keyframes per agent. Per-scene metadata (start poses, overlap matrix, semantic histogram) is shipped alongside the frames so that future work can re-roll a different split without re-rendering.

B Edge Update under Rigid PGBA Rewrites

This section derives the analytic update rule applied to an inter-agent edge measurement M_e when an agent’s PGBA refinement rigidly rewrites one of the two endpoint submaps. The rule is stated in the global pose-graph section of the main paper; here we make the assumptions and the residual transformation explicit.

B.1 Notation

A $\text{Sim}(3)$ correction $C = (s, \mathbf{R}, \mathbf{t})$ acts on a 3D point as

$$C \cdot \mathbf{p} = s\mathbf{R}\mathbf{p} + \mathbf{t}, \quad s \in \mathbb{R}_{>0}, \quad \mathbf{R} \in \text{SO}(3), \quad \mathbf{t} \in \mathbb{R}^3.$$

Composition is associative and admits an inverse C^{-1} ; we write $C_1 \circ C_2$ for the composed transform. The geometric residual of an inter-agent edge $e = (\text{src}, \text{tgt})$ with measurement $M_e \in \text{Sim}(3)$ and per-submap corrections $C_{\text{src}}, C_{\text{tgt}}$ is

$$\mathbf{r}_e^{\text{geo}} = \log(M_e^{-1} \circ C_{\text{tgt}}^{-1} \circ C_{\text{src}}) \in \mathbb{R}^7, \quad (20)$$

matching the form used in the main paper.

B.2 Rigidity Hypothesis

When agent a reports a PGBA refinement of submap \mathcal{P}_ℓ^a , every summary point shifts in a ’s local frame from $\mathbf{p}_i^{\text{old}}$ to $\mathbf{p}_i^{\text{new}}$. The rigidity check tests how well this shift is explained by a single $\text{Sim}(3)$ increment $\Delta_{a,\ell}$:

$$\Delta_{a,\ell} = \arg \min_{\Delta \in \text{Sim}(3)} \frac{1}{N} \sum_{i=1}^N \|\mathbf{p}_i^{\text{new}} - \Delta \cdot \mathbf{p}_i^{\text{old}}\|^2, \quad (21)$$

solved in closed form by the same Umeyama procedure used for inter-agent verification in the main paper. Letting $\rho_{a,\ell}$ denote the square root of the optimum of (21), the analytic edge update is invoked only when $\rho_{a,\ell} \leq \tau_{\text{rig}}$; otherwise all edges incident to \mathcal{P}_ℓ^a are invalidated and re-queued for verification. Below we derive the update under the rigid hypothesis $\rho_{a,\ell} \approx 0$, in which all summary points are jointly mapped:

$$\mathbf{p}_i^{\text{new}} = \Delta_{a,\ell} \cdot \mathbf{p}_i^{\text{old}}, \quad i = 1, \dots, N. \quad (22)$$

B.3 Analytic Edge Update

B.3.1 Measurement convention. Verification yields a $\text{Sim}(3)$ measurement M_e such that the residual (20) is minimized at the verified geometry. Equivalently, M_e is the relative transform mapping source-local coordinates to target-local coordinates,

$$M_e \cdot \mathbf{p}^{\text{src,loc}} \approx \mathbf{p}^{\text{tgt,loc}}, \quad (23)$$

for every verified correspondence pair $(\mathbf{p}^{\text{src,loc}}, \mathbf{p}^{\text{tgt,loc}})$ used in the RANSAC-ICP fit. Under (22), the local coordinates of the rewritten submap shift but the underlying physical correspondences are unchanged, so a corresponding measurement M_e^{new} must satisfy (23) in the new local frame.

B.3.2 Case I: $a = \text{src}(e)$. Every source-side correspondence shifts to $\mathbf{p}^{\text{src,new}} = \Delta_{a,\ell} \cdot \mathbf{p}^{\text{src,old}}$ while target-side correspondences are unchanged. Substituting $\mathbf{p}^{\text{src,old}} = \Delta_{a,\ell}^{-1} \cdot \mathbf{p}^{\text{src,new}}$ into (23),

$$M_e^{\text{old}} \cdot \Delta_{a,\ell}^{-1} \cdot \mathbf{p}^{\text{src,new}} \approx \mathbf{p}^{\text{tgt,loc}},$$

so the same physical correspondence in the new local frame is encoded by

$$M_e^{\text{new}} = M_e^{\text{old}} \circ \Delta_{a,\ell}^{-1}. \quad (24)$$

B.3.3 Case II: $a = \text{tgt}(e)$. Symmetrically, only target-side correspondences shift, with $\mathbf{p}^{\text{tgt,new}} = \Delta_{a,\ell} \cdot \mathbf{p}^{\text{tgt,old}}$. From (23),

$$\mathbf{p}^{\text{tgt,new}} = \Delta_{a,\ell} \cdot \mathbf{p}^{\text{tgt,old}} \approx \Delta_{a,\ell} \cdot M_e^{\text{old}} \cdot \mathbf{p}^{\text{src,loc}},$$

giving

$$M_e^{\text{new}} = \Delta_{a,\ell} \circ M_e^{\text{old}}. \quad (25)$$

Equations (24) and (25) jointly recover the analytic edge-update rule of the main paper.

B.4 Residual Consistency

We now verify that (24) and (25) are self-consistent with the corresponding rewrite of the global correction, $C_\ell^a \leftarrow C_\ell^a \circ \Delta_{a,\ell}^{-1}$, which keeps every global point invariant under (22). Substituting into (20) for Case I,

$$\begin{aligned} \mathbf{r}_e^{\text{geo,new}} &= \log((M_e \circ \Delta_{a,\ell}^{-1})^{-1} \circ C_{\text{tgt}}^{-1} \circ (C_{\text{src}} \circ \Delta_{a,\ell}^{-1})) \\ &= \log(\Delta_{a,\ell} \circ M_e^{-1} \circ C_{\text{tgt}}^{-1} \circ C_{\text{src}} \circ \Delta_{a,\ell}^{-1}) \\ &= \text{Ad}_{\Delta_{a,\ell}}(\mathbf{r}_e^{\text{geo,old}}), \end{aligned}$$

where Ad_Δ denotes the $\text{Sim}(3)$ adjoint. For Case II, the target-side increment cancels exactly:

$$\begin{aligned} \mathbf{r}_e^{\text{geo,new}} &= \log((\Delta_{a,\ell} \circ M_e)^{-1} \circ (C_{\text{tgt}} \circ \Delta_{a,\ell}^{-1})^{-1} \circ C_{\text{src}}) \\ &= \log(M_e^{-1} \circ \Delta_{a,\ell}^{-1} \circ \Delta_{a,\ell} \circ C_{\text{tgt}}^{-1} \circ C_{\text{src}}) \\ &= \log(M_e^{-1} \circ C_{\text{tgt}}^{-1} \circ C_{\text{src}}) = \mathbf{r}_e^{\text{geo,old}}. \end{aligned}$$

Thus, zero-residual edges remain zero-residual after the analytic update. For nonzero residuals, the target-side rewrite leaves the residual exactly unchanged, whereas the source-side rewrite changes its coordinates by the $\text{Sim}(3)$ adjoint. Consequently, locally well-fit edges remain consistent under the rigid rewrite, allowing the optimizer to warm-start from the rewritten state without immediately rejecting the edge. The rigidity gate $\rho_{a,\ell} \leq \tau_{\text{rig}}$ ensures that the PGBA-induced change is well approximated by a single $\text{Sim}(3)$ transform over the summary geometry. Edges failing the rigidity gate are queued for re-verification rather than analytically updated, which is what makes the update rule safe to apply in closed form rather than as part of the optimizer state.

The same construction extends to the cached anchor-image photometric payload of \mathcal{P}_ℓ^a : under (22) the anchor pose and back-projected source points are evaluated in the post-PGBA local frame, so the payload must be rebuilt; this matches the lazy-rebuild policy described in the global pose-graph section of the main paper.

C Additional Experiment

This section contains the experimental configurations referenced in the main paper and concludes with a per-scene analysis of the ReplicaMultiagent Plus comparison shown in Fig. 8 and Table 7.

C.1 Implementation Details

We implement MAGS-SLAM in PyTorch with custom CUDA kernels inherited from DROID-SLAM [43] for recurrent dense bundle adjustment and from 3D Gaussian Splatting [18] for differentiable rasterization. Experiments on ReplicaMultiagent and AriaMultiagent run on a single Intel(R) Xeon(R) Platinum 8352V host with one NVIDIA RTX 4090, while four-agent experiments on ReplicaMultiagent Plus are distributed across four Intel(R) Xeon(R) E5-2686 v4 CPUs and four NVIDIA RTX 2080 Ti GPUs (one agent per GPU, with the coordinator pinned to a fifth thread). The four parameter blocks below correspond one-to-one with the four method modules of the main paper.

C.1.1 Local per-agent monocular Gaussian SLAM. Each agent runs the DROID-based front-end with a local optimization window of 25 key-frames and the Joint Depth-Scale Adjustment term of the main paper, taking Metric3D-v2 [13] disparities as the prior $\mathbf{d}_k^{\text{prior}}$. The motion filter inserts a candidate frame whenever the predicted mean flow magnitude exceeds 2.4px, and the front-end retains it as a keyframe only if its bidirectional flow distance to the previous keyframe also exceeds 4px. Intra-agent PGBA fires whenever the loop detector returns a candidate with flow disparity below $\tau_{\text{pgba}} = 12\text{px}$ (ETH3D and Tanks-and-Temples) or 22px (Replica and Aria). A submap \mathcal{P}_ℓ^a is frozen as soon as it reaches $K_{\text{max}} = 8$ keyframes or the camera centers exceed a Euclidean distance of $\tau_{\text{move}} = 2\text{m}$. The local Gaussian map loss of the main paper uses $\alpha = 0.95$, $\beta = 0.25$, $\lambda_n = 10^{-2}$, $\lambda_s = 10$, and is optimized for 10 iterations per keyframe at base learning rates 1.6×10^{-4} for centers, 10^{-3} for scales, and 5×10^{-2} for opacities.

C.1.2 Submap summary and inter-agent verification. Each frozen submap is encoded as a 128-D mean-pooled DROID descriptor averaged over up to 3 summary keyframes selected by farthest-first sampling in pooled-descriptor cosine distance, up to $N_Q = 512$ salient 3D points scored by the main paper’s saliency formula with $\lambda_d = 0.35$ (disparity gradient) and $\lambda_F = 0.10$ (feature norm), a voxel-downsampled registration cloud (voxel size 0.05m, capped at 4,096 points), the submap AABB, and the anchor keyframe payload. Retrieval keeps the top- $K = 3$ neighbors with cosine similarity above $\tau_{\text{sim}} = 0.30$; the matcher $\Pi(\cdot; \theta_{\text{match}})$ uses absolute cosine ≥ 0.55 , ratio test ≤ 0.90 , and best/second-best margin ≥ 0.02 , falling back to LoFTR [42] between anchor images when fewer than $N_{\text{min}} = 20$ correspondences survive. Umeyama RANSAC runs for 256 iterations with a 0.15m inlier threshold, followed by ICP refinement (64 iterations, max correspondence 0.20m). The cascade verifier $V(\cdot; \theta_V)$ accepts a candidate only when at least 12 inliers survive with overlap ratio ≥ 0.25 and final residual $\leq 0.20\text{m}$, the recovered scale lies in $[0.33, 3.0]$, the ICP fitness clears $\Phi \geq 0.25$ at RMSE $\rho_{\text{icp}} \leq 0.20\text{m}$, and the spatial-extent ratio of the main paper satisfies $\eta \geq \tau_{\text{ext}} = 0.15$.

C.1.3 Global $\text{Sim}(3)$ pose graph optimization. The graph cost of the main paper uses $w^t = 5$ for intra-agent temporal edges and $w^v = 1$ for verified inter-agent edges; the anchor-image photometric term carries a per-edge gain of $w_e^{\text{pho}} = 1$ that is further normalized over the in-frame finite-depth pixels of \mathcal{U}_e , sub-sampled at stride 2 and skipped entirely when fewer than 64 valid pixels reproject cleanly. We solve the joint problem with the damped Gauss-Newton within a Levenberg-Marquardt trust region; the budget is 200 function evaluations and the remaining stopping tolerances are left at the scipy defaults. Submaps are forwarded to fusion only when their mean per-edge residual falls below $\tau_{\text{res}} = 0.2$ and they carry at least one inter-agent edge. Reactive PGBA updates apply Eqs. (24) to (25) whenever the rigidity residual of §B.2 satisfies $\leq \tau_{\text{rig}} = 0.1\text{m}$; otherwise incident edges are invalidated and re-queued.

C.1.4 Occupancy-aware fusion and refinement. The frustum-aware occupancy grid uses voxel size $v = 0.10\text{m}$, an envelope factor of $\pm 1\sigma$ on each Gaussian’s per-axis scaling for the occupied volume, ray-cast steps of $v/2 = 0.05\text{m}$ for free-space carving, 1-per-16-pixel sub-sampling along the rays, and a maximum ray length of 8m.

Joint pose-Gaussian refinement runs for 1,000 iterations at half the per-agent learning rate; the loss combines an L1-RGB term of total weight $\alpha' = 1.75$ (i.e. $(1 - \lambda) + \alpha = 0.8 + 0.95$), an SSIM term with weight $\lambda = 0.2$, an inverse-depth L1 term of weight $\beta = 0.25$ inherited from the per-agent loss, and a prior-normal cosine term with weight $\lambda'_n = 10^{-1}$ that decays to 5×10^{-2} during the final 20% of iterations. Gaussians whose opacity drops below 0.005 are pruned after refinement. Per-keyframe log-gain a_k and bias b_k are initialized at zero and optimized jointly with the camera pose deltas via Adam at learning rate 10^{-3} , so exposure compensation adapts slowly enough to absorb only inter-agent photometric drift rather than genuine geometric error.

C.2 Baselines, Metrics, and Protocol

We follow the same evaluation protocol as the main paper. Tracking accuracy is reported as Absolute Trajectory Error (ATE) RMSE in centimeters. Rendering quality is measured by PSNR, SSIM, and LPIPS. RGB-D baselines include MNE-SLAM [6], MAGiC-SLAM [53], and MAC-Ego3D [49], which are run with their official code on the ReplicaMultiagent Plus, while MAGS-SLAM runs only on the monocular RGB input. Table 7 reports ATE RMSE and rendering quality on three four-agent ReplicaMultiagent Plus scenes, Fig. 8 shows the corresponding qualitative comparison. We discuss tracking and rendering on Apartment-0, Apartment-2, and Office-2 in turn, then summarize.

C.2.1 Trajectory accuracy. Despite consuming only RGB, MAGS-SLAM achieves the lowest ATE on two of the three scenes. The gap is most pronounced on the largest-scale Apartment-0, 0.282cm against 0.594cm for MAC-Ego3D and 0.612cm for MAGiC-SLAM, because the four-agent layout repeatedly forces low-overlap inter-room transitions that magnify any residual per-agent scale drift in the RGB-D baselines, while our Sim(3) submap pose graph absorbs the drift at the submap boundary. On Office-2, which mixes a long corridor with two cluttered rooms, MAGS-SLAM still leads with 0.354cm versus 0.395cm for MAGiC-SLAM and 0.485cm for MAC-Ego3D. Apartment-2 is the one scene where an RGB-D system wins, MAC-Ego3D at 0.329cm versus our 0.404cm, because its dense thin-structure layout (chair legs, bookshelf verticals) provides exactly the high-frequency depth gradients that direct depth measurement resolves more cheaply than monocular priors.

C.2.2 Rendering quality. Across all three scenes, MAGS-SLAM holds the top rank on PSNR, SSIM, and LPIPS jointly, with a uniformly large margin over the strongest RGB-D entry: Office-2 with 40.19dB versus 32.17dB for MAC-Ego3D (+8.0dB), Apartment-0 with 40.86dB versus 27.09dB for MAGiC-SLAM (+13.8dB), and Apartment-2 with 41.07dB versus 27.50dB for MAC-Ego3D (+13.6dB). LPIPS drops by roughly an order of magnitude on the two apartment scenes, indicating perceptually visible improvements rather than residual photometric tuning. Inspecting Fig. 8, two consistent failure modes drive the RGB-D gap. First, MAGiC-SLAM and MAC-Ego3D place duplicated Gaussian shells along bed and shelf edges, where two agents observe the same surface from incompatible scales; the occupancy-aware fusion of the main paper collapses these into a single consistent shell. Second, the smaller relative PSNR gain on Office-2 (+8.0dB) is consistent with Office-2 being

the easiest of the three trajectories for the RGB-D baselines, its room being geometrically rich and well-overlapped at the endpoints.

C.2.3 Summary. Across Apartment-0, Apartment-2, and Office-2, MAGS-SLAM is at worst within sub-centimeter ATE of the strongest RGB-D method and is uniformly first on every rendering metric, with PSNR margins of +8.0dB to +13.8dB. This pattern substantiates the central claim of the paper, that an explicit Sim(3) treatment of the inter-agent geometry, combined with geometric and photometric optimization and occupancy-aware fusion, is sufficient to close the depth-sensor gap on a benchmark designed to expose it.

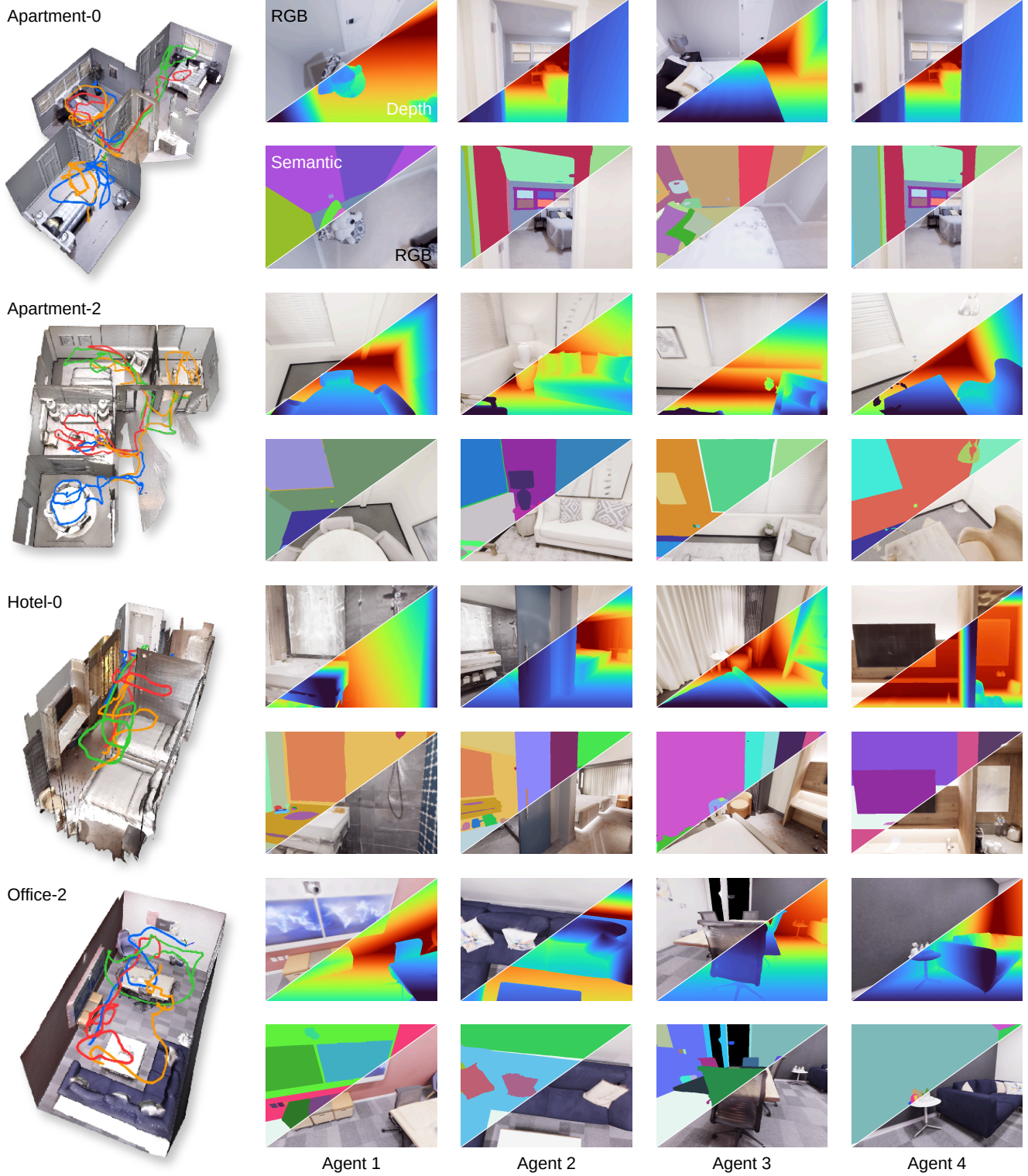


Figure 7: 4 examples from the ReplicaMultiagent Plus benchmark. Each row shows a scene with four agent trajectories (colour-coded) and the associated per-pixel semantic ground truth. Configurable overlap lets the same scene be rendered as cleanly disjoint or heavily overlapping multi-agent splits without re-running the simulator.

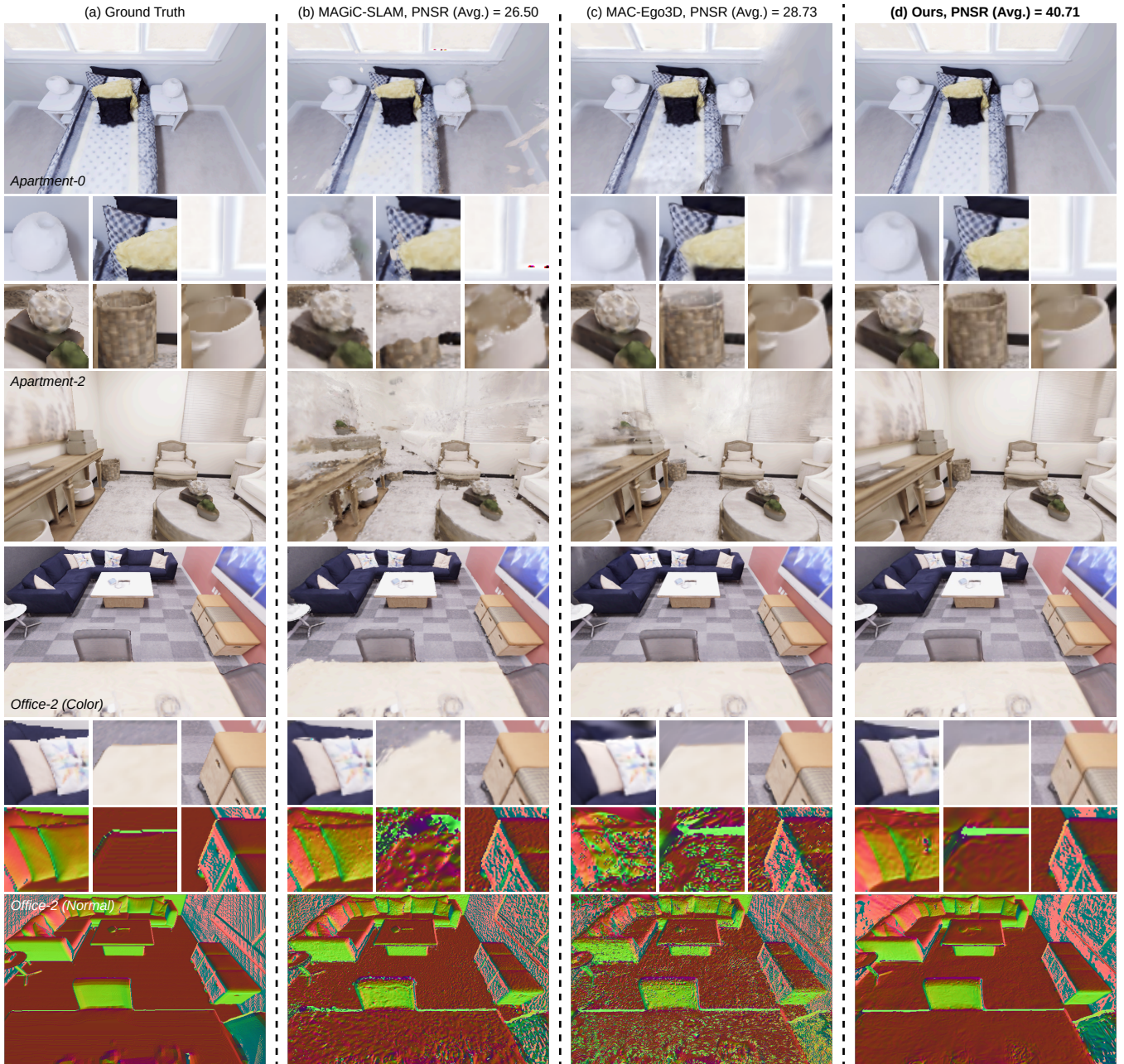


Figure 8: Qualitative comparison of multi-agent reconstruction on our proposed ReplicaMultiagent Plus dataset.

Table 7: Multi-agent tracking accuracy comparison (ATE RMSE [cm] ↓) and rendering quality comparison (PSNR/SSIM/LPIPS ↑↓) on ReplicaMultiagent Plus datasets. † indicates that CP-SLAM does not support settings with more than two agents. Best results are highlighted as **first**, **second**, and **third**.

Method	Input	Office-2 (4 Agents)				Apartment-0 (4 Agents)				Apartment-2 (4 Agents)			
		ATE ↓	PSNR ↑	SSIM ↑	LPIPS ↓	ATE ↓	PSNR ↑	SSIM ↑	LPIPS ↓	ATE ↓	PSNR ↑	SSIM ↑	LPIPS ↓
MNE-SLAM [6]	RGB-D	0.508	27.71	0.907	0.203	0.974	25.46	0.883	0.218	0.614	23.27	0.756	0.402
MAGiC-SLAM [53]	RGB-D	0.395	31.37	0.969	0.101	0.612	27.09	0.909	0.188	0.365	21.04	0.762	0.366
MAC-Ego3D [49]	RGB-D	0.485	32.17	0.955	0.071	0.594	26.53	0.929	0.198	0.329	27.50	0.929	0.198
MAGS-SLAM (Ours)	RGB	0.354	40.19	0.988	0.028	0.282	40.86	0.992	0.013	0.404	41.07	0.990	0.018

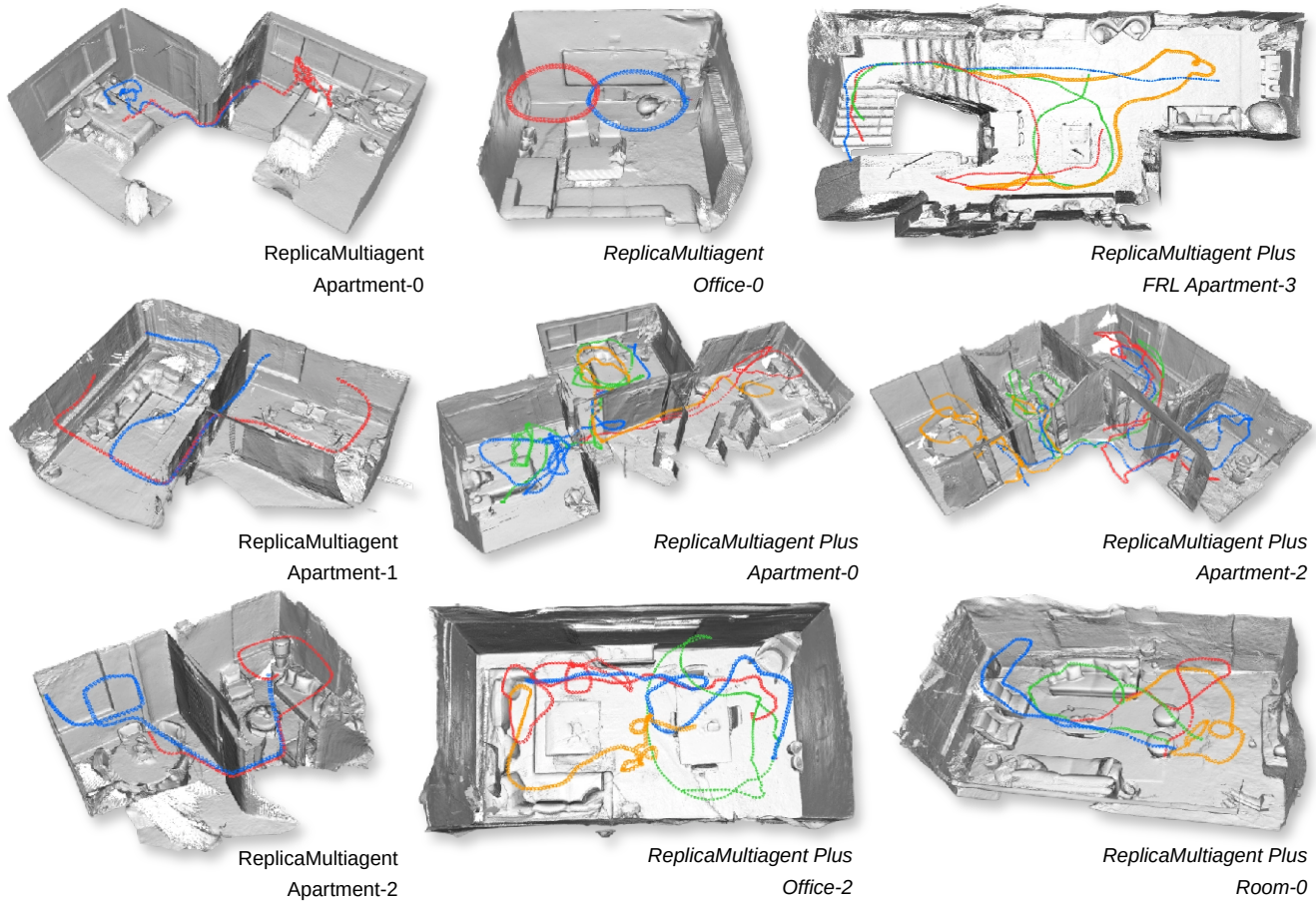


Figure 9: Qualitative results of MAGS-SLAM on the ReplicaMultiagent [12] dataset and ReplicaMultiagent Plus (ours) dataset.

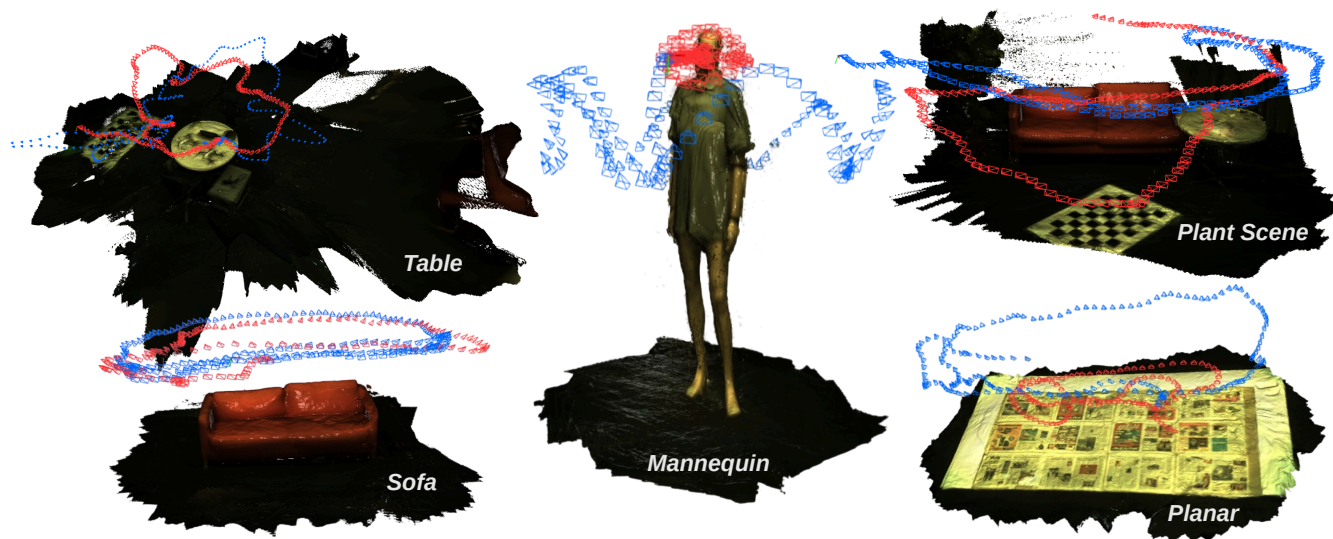


Figure 10: Qualitative results of MAGS-SLAM on the real-world indoor ETH3D [39] dataset.

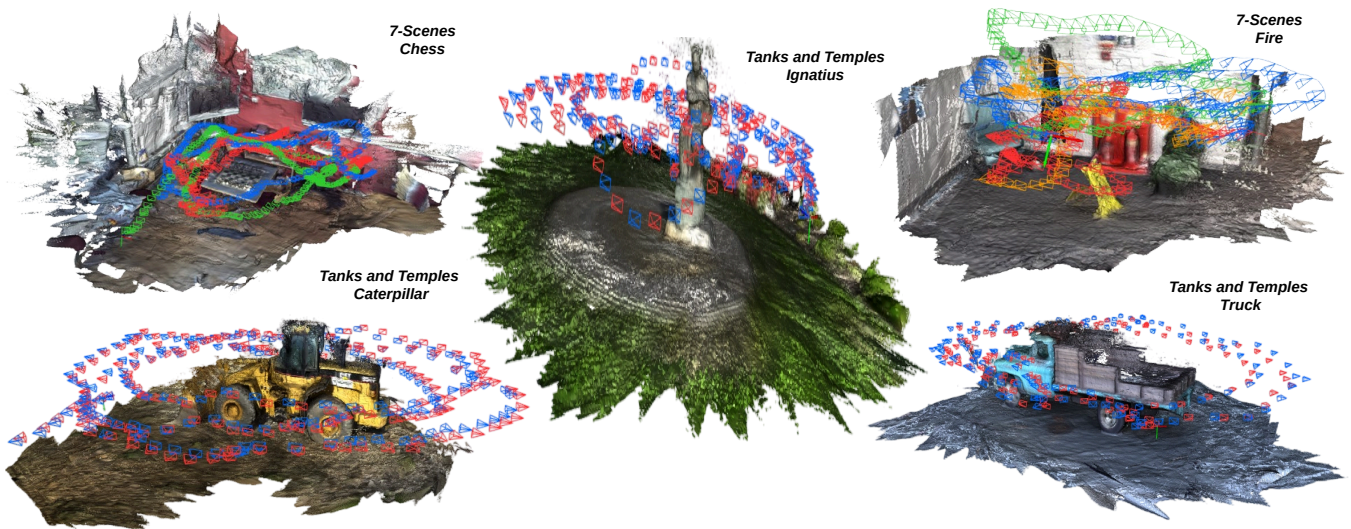


Figure 11: Qualitative results of MAGS-SLAM on the real-world indoor 7-Scenes dataset [9], and real-world outdoor Tanks and Temples [19] dataset. For the Tanks and Temples dataset, the two agent trajectories are formed by interleaved frame splitting.